

# AEROMECHANICS OF A COAXIAL MARS HELICOPTER USING HIGH-FIDELITY CFD/CA

**Daniel Escobar**  
Graduate Research Assistant  
descobar@umd.edu

**Inderjit Chopra**  
Distinguished University  
Professor  
chopra@umd.edu  
Alfred Gessow Rotorcraft Center  
University of Maryland  
College Park, MD, USA

**Anubhav Datta**  
Associate Professor  
datta@umd.edu

## ABSTRACT

A high-fidelity coupled computational fluid dynamics (CFD) and comprehensive analysis (CA) solver is developed for application on the Mars helicopter. Accurate aeromechanical understanding of a coaxial rotor on Mars is necessary in order to make proper design decisions for future aircraft with longer range and greater payload. The objectives are to understand the performance, structural loads, control loads (pitch link), wake interaction, and blade strike for hingeless and articulated coaxial rotors, so that an informed decision between the two rotor hubs can be made. This will become more important as the vehicle size and payload grows. Lower fidelity tools are not capable of capturing the complex flow phenomena (blade vortex interaction, roll-up and core growth, and 3D unsteady pitching moments at low Re), and therefore this problem requires coupled CFD/CA. Some of the key conclusions specific to Mars are: (1) an articulated rotor in fact benefits from greater rotor separation because pitch angles, not flapping motion dictates separation (2) a hingeless rotor experiences only marginally greater (6–7%) flap bending moments compared to an articulated rotor, (3) the oscillatory pitch link loads on an articulated rotor are nominally 15.5% greater than on a hingeless rotor and (4) the steady pitch link loads of a hingeless rotor are in fact 8 times greater than an articulated rotor. For these reasons, larger future Mars helicopter it appears an articulated rotor might be more desirable over a hingeless rotor, for considerations of structural and control loads.

## 1. INTRODUCTION

NASA's Mars 2020 mission is set to land on Mars on February 18th, 2021, and will be launched from Earth aboard an Atlas V rocket. The rocket will be carrying the 2315 lb (1050 kg) Mars 2020 Rover, and aboard the rover, attached to the underbelly, will be a 4.0 lb (1.8 kg) Mars Helicopter Scout. A culmination of nearly three decades of study, the Mars Helicopter Scout marks humankind's first attempt of extraterrestrial flight. Many recent advances in VTOL and micro-aerial vehicle (MAV) technology has primed aerial exploration of Mars via rotary-wing flight. Robust and reliable micro electronics, greater understanding of MAV aerodynamics, compact power sources, autonomy, and advanced control have made the possibility of flying on Mars a possibility. With successful flights on Mars, scientific horizons will expand dramatically, and open countless possibilities for future missions, for larger aircraft with greater range and payload.

### 1.1. Motivation

Over the many decades spent on the planet, the Mars rovers have collectively covered less than 40 miles.<sup>[1]</sup> The terrain explored has been relatively smooth, flat, and open, avoiding any potentially dangerous or inaccessible targets such as caves, gullies, craters, or slopes, as seen in figure 1. Scouting with a rotorcraft, would increase the scope

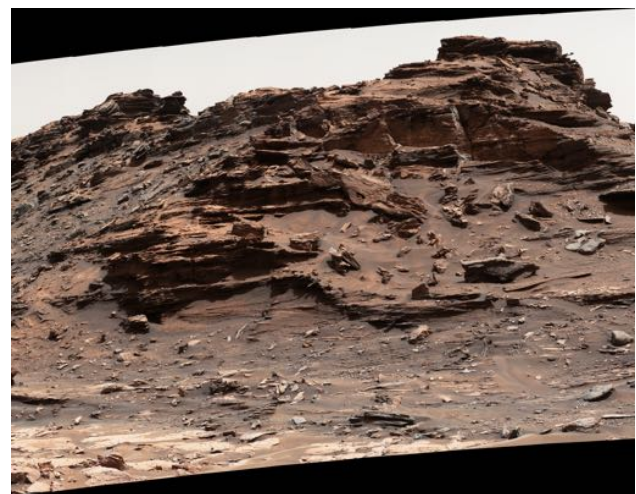


Fig. 1: Inaccessible Rocky Martian Terrain

and range of exploration, and provide easier and safer access into caves, craters, ice, and up along slopes. In addition to the exploratory data collected by the airborne sensor suite, aerial mapping could study terrain deemed too treacherous for the ground rover, speeding up ground travel and avoiding any potential catastrophes for the rover. Due to the thin atmosphere and jagged terrain, fixed wing aircraft must maintain a high velocity. They also pose significant launch and recovery challenges. Due to high gusts in the Martian atmosphere, lighter-than-air aircraft could not be controlled to station keep at specific locations of interest. A rotorcraft also offers the capability of multiple return-to-rover flights. Only a rotorcraft can fly at low speeds and

Presented at 45th European Rotorcraft Forum, Warsaw, Poland, 17-20 September, 2019 This work is licensed under the Creative Commons Attribution International License (CC BY). Copyright © 2019 by author(s).

hover. A coaxial rotorcraft can be ideal because of its compact design, efficient hover, good gust tolerance, and relatively high blade Reynolds number ( $Re$ ) within a fixed budget of weight and volume. Single main rotors require a tail rotor which adds volume and packaging concerns. Multirotors have a higher empty weight fraction due to the structure and cannot achieve the same Reynolds number as a coaxial rotorcraft for a given volume.

Our understanding today is adequate to hop in to the Mars atmosphere and fly for a short while, but the possibilities in the future can be limitless, through careful and systematic understanding of aeromechanics on Mars. Therefore, the principal purpose of this research is to collect and document systematic experimental results, and develop a high fidelity aeromechanics analysis. For such a unique case, with no prior database for guidance, predictive models must be validated by experimental data.

## 1.2. Challenges

The Martian environment presents a unique and challenging set of design requirements. The thin carbon dioxide atmosphere, with a density of only 1.36% of Earth yet a speed of sound as high as 72% of Earth, can place the rotors in a simultaneously very low Reynolds number ( $< 10,000$ ), and relatively high tip Mach number ( $M$ ) ( $> 0.3$ ) conditions.<sup>[2]</sup> Hence the flow is influenced by both viscous and compressibility effects. Due to the poor aerodynamic performance associated with such flows, optimizing both weight and performance are crucial for sustained flight with a meaningful payload. The very low density leads to very low Lock numbers and therefore very low aeroelastic damping. Aerodynamic flap damping, taken for granted on Earth, to a large extent disappears on Mars. Large rotors, to counter the low Reynolds number, and a light weight airframe increase to the danger of rotor-body frequency coalescence. The thin atmosphere also means that there is little convective cooling for the motor or other components. However, there are several advantages on Mars that can be harnessed and exploited. The gravitational acceleration is only 37.3% of Earth which significantly reduces the thrust requirements. The high rotational speeds prompted by low Reynolds number produce very low advance ratios, which is advantageous for avoiding blade strike for a coaxial rotor. Flying on an uninhabited planet means that there are no restrictions on noise or concerns for operator safety.

The aeromechanics of Mars quickly deviates from Earth for several reasons: (1) the very low Lock number (0.03 – 0.08) resulting in aerodynamic flap damping one to two orders of magnitude lower than Earth, (2) significant pitching moments and control loads from a cambered plate airfoil at unusually high rotational speeds and chordwise center of gravity (C.G.) offset, and (3) rotor and fuselage frequency coupling for large rotor blades with a small, soft, symmetric fuselage.

The very low Lock number has a positive effect on aeroelastic stability, however, the lack of aerodynamic damping will cause undamped flapping. One way to mitigate the number of flapping cycles is to use a stiff hingeless rotor, which also avoids ground resonance, but produces high hub moments. The high hub moments are good for controls but bad for weight, particularly for larger aircraft of



Fig. 2: Coaxial Mars Rotorcraft Design

the future. The high rotational speeds produce high cyclic stresses, which for hingeless rotors means a heavy rotor. The combination of a heavy rotor and a light airframe increases the danger of fuselage coupling with the rotor. Another option would be to use an articulated rotor, that would relieve the loads, but would require a mechanically complex hinge, greater rotor separation to accommodate for larger flap angles, but less hub moments for controls. The hingeless rotor would also provide improved handling qualities.

The blade pitching moments, associated with the high chord lengths and control angles, are potentially high. Additional unsteady pitching moments at very low Reynolds number and high Mach number, with added three dimensional effects from low aspect ratio blades, are also unknown. The loads from high pitching moments could be too high for the control system of a small aircraft, and must be properly accounted for. Understanding rotor loads, especially these control loads, and the ability to predict them are crucial for the optimum design of a lightweight vehicle. The shaft, actuators, control rods, swashplate, and pitch links of the control system can be properly designed only if the vibratory loads can be correctly predicted. For these unique aeromechanical conditions, designers have little experience or guidance, either experimental or analytical. There have only been limited studies on a small scale Mars rotorcraft on the scale of 200 g to 50 kg<sup>[3–5]</sup> except for a recent MHS design, which is largely unpublished except for a few recent papers.<sup>[6,7]</sup>

## 1.3. Related Work

The concept of exploring Mars with a small-scale aerial scout was first presented decades ago by Savu and Trifu.<sup>[8]</sup> This and much of the early work on this concept were feasibility studies, using crude momentum theory to justify the idea. The goal was to prove enough lift could be generated by a rotor in the thin Mars atmosphere. Additionally, the significant scientific benefits and the concept of operations of the aircraft were outlined.<sup>[8,9]</sup> After the initial feasibility studies, experimental work began and more detailed analysis was developed and carried out.<sup>[2,3]</sup> Young et al. utilized the the NASA Ames Planetary Aeolian Laboratory's vacuum chamber to perform hover testing investigations of a conceptual Mars rotorcraft. A 4 ft (1.219 m) radius isolated four bladed rotor was tested and showed that the con-



Fig. 3: NASA Ames proof-of-concept Mars rotor hover test stand<sup>[2]</sup>

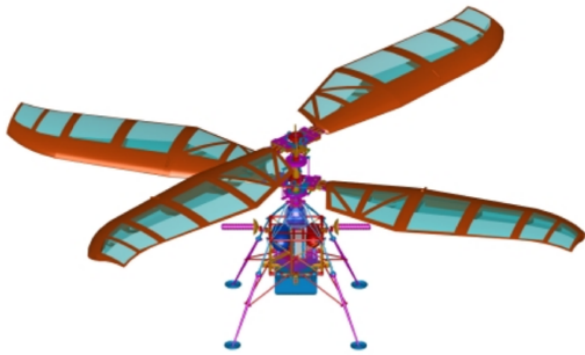


Fig. 4: University of Maryland 2000 Student Design Competition winning submission, MARV<sup>[10]</sup>

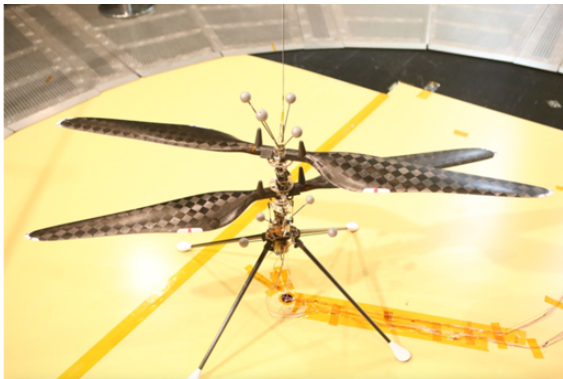


Fig. 5: NASA JPL's Mars Helicopter Scout<sup>[6]</sup>

cept rotor was capable of reaching the design thrust goals. Additionally, a coaxial hover test rig was built for Ames Research Center low-pressure environmental chamber for performance testing, with the goal of conversion into a flight demonstrator.

One of the first detailed design study was carried out by Datta et al., at the University of Maryland, that demonstrated the quantitative merits of a 110.2 lb (50 kg) 2-bladed coaxial Mars helicopter.<sup>[3,10]</sup> This report was a detailed study into the entire vehicle design. Investigations of key vehicle components and rotor parameters were conducted. Rotor configurations, including single main rotor, quad ro-

tor, and tilt-wing among others, were considered and trade studies found a coaxial rotor was the best choice due to energy requirements, low Reynolds number conditions, and vehicle size and compact folding. The rotor aerodynamic design was parametrically investigated and found a unique high solidity, twisted, and tapered rotor with a new high lift airfoil, with very gradual pressure recovery, was best for the Mars operating conditions. The blade structural design utilized a light weight box beam spar, to reduce the weight while still supporting the bending loads, and incorporated blade folding mechanisms. A teetering hub was chosen to reduce the vibratory loads. Due to the lack of oxygen in the Martian atmosphere, a range of novel power plants were considered including fuel cells, electric batteries, solar, hydrazine and  $CO_2$  breathing engines. The proton exchange membrane fuel cells were chosen due to their minimum system weight and large potential for improvement in the coming years. The report also outlines the design of the power train, fuselage structure, landing gear, control system, and avionics. A concept of operations was described that included a blade folding mechanisms, arrangement within the aeroshell for landing on Mars, deployment, and flight operations.

Since then, greater understanding of the unique aerodynamics has been gained through small scale low Reynolds number testing and computational fluid dynamics (CFD) analysis.<sup>[4,5,11]</sup> Winslow et al. found that compared to any airfoil thin cambered plates in fact provide optimal hover performance, measured as Figure of Merit, in the target Reynolds number range of a small scale Mars helicopter. Keeping the airfoil as thin as possible is best, and a sharp leading edge is advantageous to trip the laminar separation bubble in the low Re flows and keep the flow attached over most of the chord. Using the low Reynolds number airfoils, Shrestha et al. performed vacuum chamber hover testing for a small aircraft, less than 2.2 lb (1 kg), and achieved a maximum Figure of Merit of 0.62. The rotor used had a radius of 9.2 in (0.23368 m) and a pitched pitch cantilevered hub mounting. Through the use of CFD analysis, Corfeld et al. found significant influence on rotor aerodynamics from three dimensional (3-D) effects, such as stall modification due to rotation, and strong root and tip vortices. 2-D sectional aerodynamic analysis is not sufficient to accurately model Mars rotor designs.

More recently, work has been conducted at the NASA Ames Research center covering both experimental testing and analytical computations. Both single and dual, co-rotating, rotors were tested in forward flight in the Martian Surface Wind Tunnel, part of the Planetary Aeolian Laboratory. Rotor performance data was collected and compared with predictions calculated using a momentum disk based low fidelity 3-D CFD code Rotorcraft CFD (RotCFD). At Mars atmospheric conditions, the analysis over predicted the measured torque values. Additionally, Koning et al. developed a comprehensive analysis (CA) model, using CAM-RADII, of the Mars helicopter using C81 tables to generate the aerodynamic data at low Reynolds numbers and successfully predicted the JPL Mars Helicopter hover test data.

Work on the JPL Mars Helicopter Scout has begun to be published over the past couple years. Most of the published work focuses on the flight dynamics, navigation, and autonomy of the aircraft and not on the aeromechanics, perfor-



mance, or loads. Stable free-flight hover using closed loop controls of the engineering development models (EDMs) in the JPL 25-ft Space Simulator show successful implementation of the flight control software, and avionics hardware.<sup>[12]</sup> The JPL developed software HeliCAT was used for flight control modeling and simulation. Additionally, hover and forward flight tests of a commercial aircraft fitted with the Mars Helicopter flight avionics and navigation sensors were successful using the vision-based navigation.<sup>[13]</sup> A detailed explanation of the vehicle components, construction by Aerovironment, Inc., and hardware testing was presented by Pipenberg et al.<sup>[14]</sup> The structural testing was to ensure the vehicle could survive the high loading conditions of travel to Mars, including launch and touch down.

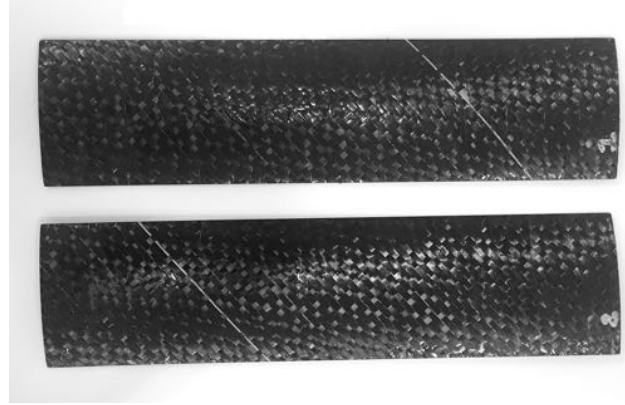
#### 1.4. Description of Content

In the following sections, first, an objective aircraft is described, which is the design basis for the rotor used in the experimental testing and computational predictions. This is followed by descriptions of both the vacuum chamber rotor rig development and experimentation, and the computational analysis developed and validated. As part of this work, both a baseline comprehensive analysis using lifting line aerodynamics and coupled high fidelity CFA/CA analysis are implemented. Once the structural and aerodynamic properties have been verified with the hover data, coaxial forward flight trim analysis is carried out. The effect and need to use high fidelity analysis for this unique and complex problem is investigated and discussed. Then the analysis is used to investigate the effect of hub type, hingeless and articulated, on the rotor performance and loads.

Highlighted by the unique challenges of rotary wing flight in the Mars atmosphere, including the travel to Mars, designing a vehicle as light as possible is a major design driver. In order to achieve a lightweight design, the expected rotor loads need to be predicted so that the rotor blades and hub can be built as light as possible. During the design process, one of the most important decisions is the rotor hub type, which is conventionally either articulated or hingeless. An articulated rotor has a flap hinge to allow for both rigid and elastic flap motion. Since the hinge cannot support any moments, this design relieves the flap bending loads, but this results in a greater flap angle and a complex hub requiring hinges. A hingeless hub eliminates the flap hinge and only allows for elastic flapping. The hingeless hub therefore carries greater loads, but reduces mechanical complexity. The root bending moments are proportional to the first flap frequency. For conventional aircraft, articulated rotors have a first flap frequency around  $\nu_\beta = 1.05/\text{rev}$  and hingeless rotors around  $\nu_\beta \geq 1.15/\text{rev}$ . For application on Mars there are many other considerations. The purpose of this paper is to investigate the effects of the rotor hub type on rotor performance and loads so that an informed decision can be made. Low order models have been proven effective in predicting rotor performance, but due to the complex aerodynamic environment of a multirotor on Mars, higher fidelity analysis is necessary to predict the loads. Lower order models cannot capture the true nature of 3D unsteady vortical flows, blade vortex interactions, and unsteady blade pitching moments. For these reasons, a CFD/CA coupled analysis is essential. The purpose of this paper is to carry out this task.



(a) Cross section of 6% camber 2% thick composite rotor blades



(b) Planform of 2 in chord and 9.2 in radius composite rotor blades

Fig. 6: Views of the geometry of composite rotor blades for Mars rotor

Table 1: Mars Model Rotor Description

Number of Blades	2
Rotor Diameter	18.4 in (0.4674 m)
Root Cut-Out	13%R, 1.23 in (0.0313 m)
Airfoil	6% Camber 2% Thick Cambered Plate
Chord	2 in (0.0508 m)
Twist	Zero
Taper	Zero
Solidity	0.1384
Lock number	0.067
Rotational Speed	2,400 RPM
Weight (blade)	0.02 lb (9.15 g) per blade

#### 1.5. Objective Aircraft and Rotor

The objective aircraft is a small, 0.2 kg coaxial rotorcraft, based on a scaled version of MARV, the University of Maryland 2000 AHS Design.<sup>[3]</sup> Figure 2 shows a CAD rendering of the aircraft. Each rotor is two bladed with an 9.2 in (0.2337 m) radius and 2 in (0.0508 m) chord. The rotor has a solidity of 0.1384. The rotor has pitch bearing at 0.06  $R$ , a root cut out of 0.13  $R$ , and the blade cuff at 0.16  $R$ . At the design condition, the rotor operates with tip Reynolds number below 10,000 and a low tip Mach number of around 0.17. The blades have no twist or taper, and have a cambered plate airfoil, with 6% camber and 2% thickness. The airfoil design is guided by previous experimental studies for the most favorable aerodynamic performance in these adverse conditions.<sup>[5]</sup> A summary of the rotor is presented in Table 1.

## 2. METHOD

The objective of this paper is to investigate the coaxial Mars rotor by developing a high fidelity coupled CFD/CA analysis. For such a unique case, any analysis must be validated



Fig. 7: Vacuum Chamber Exterior

piece-wise with experimental data for accuracy. Performance data was measured in experimental tests and used to validate a single rotor comprehensive analysis model. Then the analysis was extended to a coaxial rotor in forward flight with both hingeless and articulated hubs. Then the comprehensive analysis was coupled to high fidelity 3-D CFD in order to capture the complex flow phenomena associated with a coaxial rotor and the Mars atmosphere. Presented here is the development of the coupled CFD/CA tool and a detailed analysis of rotor hubs by studying sectional airloads, blade loads, pitch link loads, and performance.

## 2.1. Vacuum Chamber Set-up

The experimental setup built for this research is an extension and improvement over the previously presented work [15,16]. The setup includes a vacuum chamber system, data acquisition system, hover stand, sensors, and an isolated single rotor. The goal of the testing presented here is to collect rotor performance, but more importantly unsteady hub loads and pitch link loads.

The test stand is placed inside a custom built 3 ft diameter cylindrical vacuum chamber. It is equipped with pressure and temperature sensors to calculate the operating atmospheric conditions, Reynolds and Mach number. The hover stand was constructed from stainless steel Maker-Beam and an aluminum plate for mounting to the rotor. The rotor is mounted on a custom 3D printed ABSplus plastic mount which holds the rotor, motor, and linear actuators. The hover stand places the rotor 2.4 radii above the bottom of the chamber to ensure the rotor is out of ground effect. The rotor thrust, torque, and hub forces and moments are measured using an ATI Nano 43 six-axis force and moment transducer, the rotor rotational speed is measured using an optical tachometer, and the pitch link loads are measured

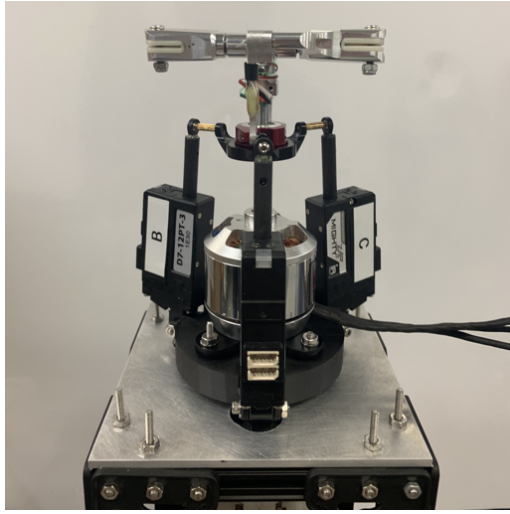
by instrumenting one of the pitch links with strain gauges. The rotor has full cyclic controls through a swashplate and linear actuators.

The development of the original test rig is described in [15,16] only the most significant recent changes to the test stand are highlighted. The ATI Nano 17 is replaced by the ATI Nano 43 load cell, which increases the maximum load and sensing range capability by a factor of 100% while also improving the data resolution by 60%. Additionally, the ATI Nano 43 importantly includes a through hole, which is necessary for the rotating frame pitch link load measurements.

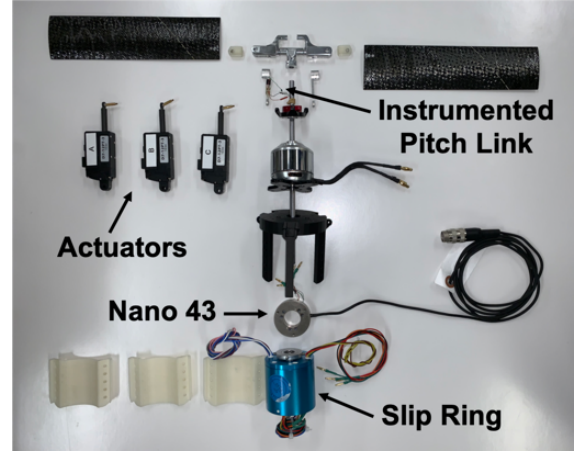
The pitch links were instrumented to measure the axial strains. This was achieved by constructing pitch links with a square cross section of  $1/8$  in by  $1/8$  in, then instrumenting them with two Omega Transducer Quality Dual Element 90° Biaxial Tee Rosette Strain Gauges. Each tee rosette contains two strain gauges and the combination is set up as a full Wheatstone Bridge configuration as to measure the axial strain while compensating for both temperature and superimposed bending strains. An instrumented pitch link is shown in figure 10. The pitch link was then calibrated with axial loads, as shown in figure 9a, upto 500 g, at 50 g step sizes. The data for three separate trials is shown in figure 9b. The data was fit to a linear regression model and found to have an  $R^2$  value of 0.996. The pitch links are in the rotating frame. To collect the rotating frame data and transmit it to the fixed frame, a slip ring was used. The slip ring, shown in figure 8, has twelve channels and is rated up to 5000 RPM. The main shaft is replaced with a slightly larger outer diameter main shaft that is hollow; this required the use of a new motor. The pitch link wires are fed into the main shaft through a hole near the base of the rotor hub. Then the wires travel down through the swashplate, motor, and slip ring, and then can the output of the slip ring is in the fixed frame. To ensure all the rotor forces, both hub and pitch link, are carried through the load cell and there are no additional load paths, a 3-D printed stand was implemented so that the motor and all three pitch actuators are mounted on top of the load cell and the slip ring is suspended from the same printed mount, with no contact with the aluminum hover stand plate.

The micro rotary servos used for pitch actuation were replaced by Trossen MightyZap linear actuators. The linear actuators have a maximum force of 12 N, and a 30 mm stroke length with 0.1 mm positional accuracy. Calibration was conducted to map the servo position to blade pitch angle, results are shown in figure 11. The servos are capable of 0.1° accuracy.

The rotor has been tested at a range of tip Reynolds numbers between 3,000 and 10,000 at a constant tip Mach number of 0.09. The Mach number was fixed by rotor speed. The Re conditions were achieved through varying chamber pressure. At each condition, collective pitch was swept from  $-10^\circ$  to  $40^\circ$ , at  $5^\circ$  increments, all with zero cyclic input. The collective sweeps resulted in blade loadings,  $C_T/\sigma$ , of roughly  $-0.12$  to  $0.22$ . Additionally, at tip Re of 4,600 and 10,000, for three different collective settings,  $5^\circ$ ,  $10^\circ$  and  $15^\circ$ , cyclic inputs of  $1^\circ$  and  $2^\circ$  were input to provide an unsteady pitching moment while in hover.



(a) Hover test stand

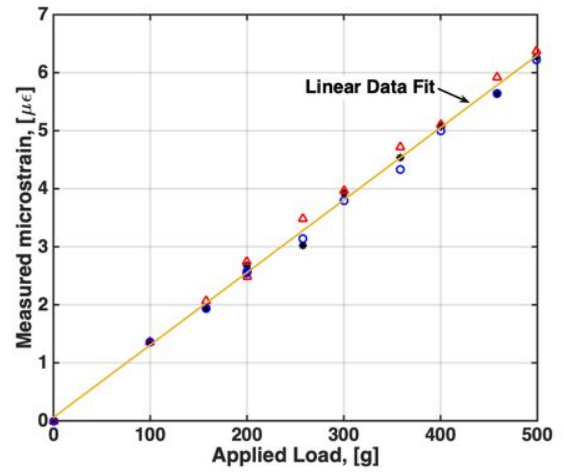


(b) Disassembled experimental setup

Fig. 8: Experimental test rig setup



(a) Pitch link calibration of axial load experimental setup



(b) Pitch link calibration data with linear fit

Fig. 9: Pitch link calibration setup and results



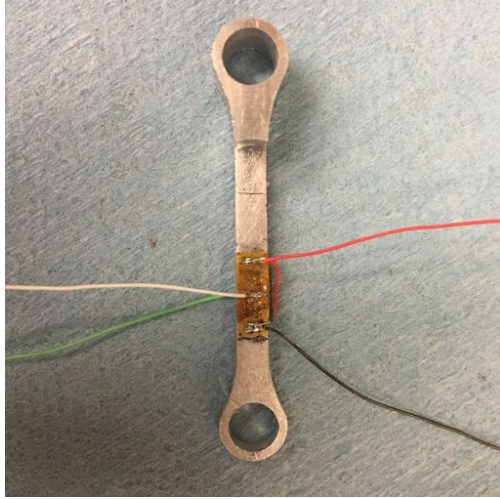


Fig. 10: Instrumented pitch link, with full Wheatstone bridge strain gauge configuration

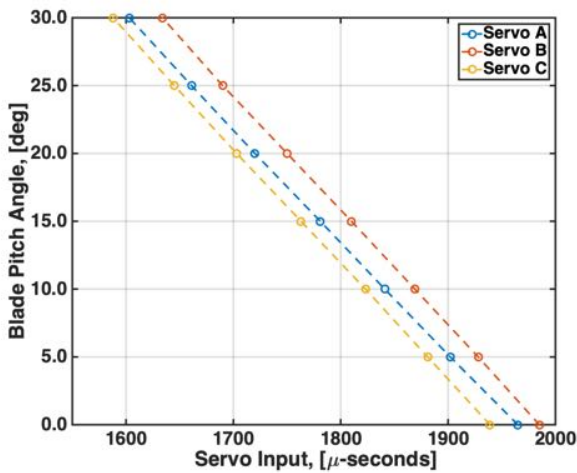


Fig. 11: Swashplate servo calibrate curves

## 2.2. Comprehensive Analysis

The University of Maryland Advanced Rotorcraft Code (UMARC) was used to carry out a comprehensive analysis of a hingeless and an articulated (flap-only), coaxial rotor including flexible blades, unsteady aerodynamics, free-wake, and coaxial trim (torque balance). The aerodynamics use Weissinger-L lifting line with a time accurate free-wake. Airfoil properties are determined by a range of  $\pm 180^\circ$  CFD look-up tables, which account for spanwise Reynolds number distribution. For all the cases, the free wake contained three turns. The rotor blades are modeled as second order, nonlinear, Euler-Bernoulli beams. The coaxial rotor model uses a six degree of freedom trim for individual rotor thrust, zero lateral and longitudinal moments, and zero total system torque. A target thrust of  $C_T/\sigma = 0.08$  is held constant throughout all the coaxial rotor cases. The analysis was conducted with a nose down shaft angle of  $\alpha = 5^\circ$ , and a modest advance ratio of  $\mu = 0.10$ , which corresponds to a forward velocity of  $11.4 \text{ knots}$  ( $5.87 \text{ m/s}$ ). A simpler single rotor analysis, the same model as the coaxial, but with one rotor, was used to validate with experimental data. For blade loadings,  $C_T/\sigma$ , of roughly  $-0.08$  to  $0.22$  the comprehensive

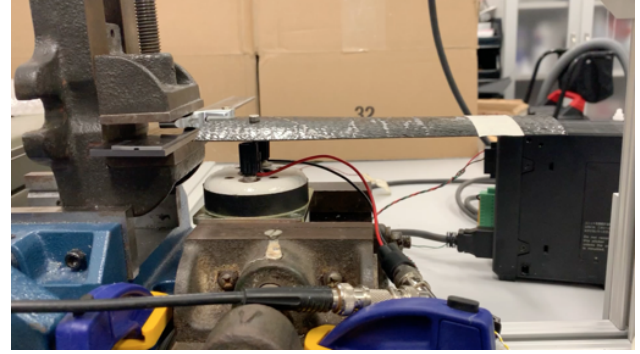


Fig. 12: Experimental shake test for measurement of non-rotating frequencies

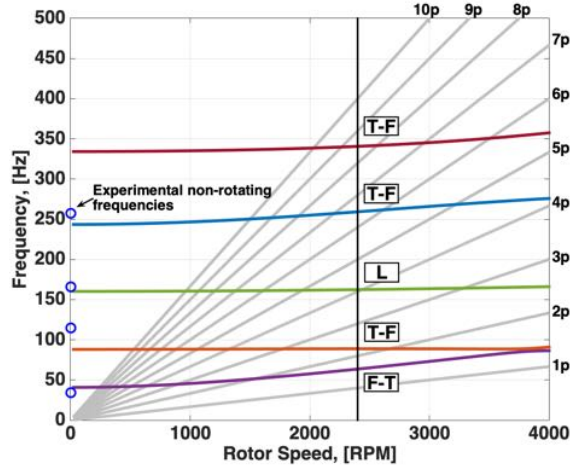
analysis well predicted the experimental results and trends for performance and stall onset, with a slight under prediction of maximum Figure of Merit. The model of the coaxial rotor is identical to this validated single rotor model, other than increasing operating RPM to 2,400, to match the objective aircraft, up from 1,000 RPM, at which the tests were conducted. The lower RPM produces lower  $Re$  and hence more conservative (restrictive) validation of aerodynamics.

## 2.3. Comprehensive Analysis Blade Properties

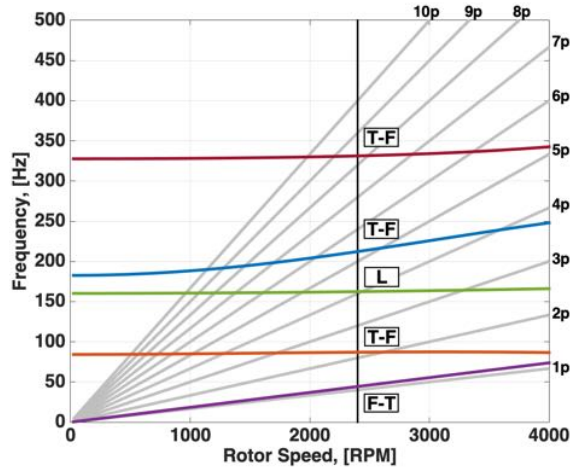
The UMARC model rotor structural and aerodynamic properties are derived from experimental rotor testing and computational tools, respectively. The experimental blades are made of carbon fiber composites and oven cured, shown in figure 6. The blade structural properties were found by experimentally measuring the flap stiffness and using the data to tailor the material properties of a model in the three-dimensional structural solver, X3D, to find the chordwise and torsional properties. A more detailed description of the blade manufacturing and property extraction process can be found in [15]

In addition to the stiffness properties, the non-rotating frequencies of the blade were experimentally measured with a shake test. The rotor hub was disassembled so that the blade grip could be used to hold the blade so that the shake tests would have the same boundary condition as used in the vacuum chamber testing. The blade grip was clamped and secured to the ground, as to provide a hingeless rotor boundary condition. A shaker was then used to actuate the blade close to the root,  $20\%R$ , and the deflection response close to the tip,  $80\%R$ , was recorded using a laser height gauge. The shaker swept through input frequencies of  $10\text{Hz}$  to  $300\text{Hz}$ , and an FFT of the deflection response gave the non-rotating natural frequencies of the blade. The experimental setup is shown in figure 12. The first four frequencies were measured and are shown in the hingeless fan plot, figure 13a. The fifth mode is above the tested range, and therefore not captured.

With the structural properties of the rotor blades known, UMARC was used to calculate the rotational frequencies for both the hingeless and articulated rotor hubs, which are shown in figure 13 as fan plots. Between the two hubs the largest difference is in the first frequency, while the higher modes show very similar trends. The first mode is a flap-torsion coupled mode, dominated by flap motion. The second, fourth and fifth modes are all also flap-torsion coupled



(a) Hingeless Fan Plot



(b) Articulated Fan Plot

Fig. 13: Fan plots for both hingeless and articulated rotor hubs, both with 13.3% root cut-out

modes, but are dominated by torsional motion with small flap deflection. The second frequency is a pure lag mode. These modes are the same for both the hingeless and articulated rotors. At 1,000 RPM, the rotational speed of the hover test, the blade is very stiff with the first flap frequency nearly at 3/rev, but at the higher rotational speed of 2,400 RPM, where the Mars helicopter is expected to operate, the first flap mode is more typical of a stiff hingeless rotor (1.58/rev). The articulated rotor has a first flap frequency of 1.11/rev.

A computational study was conducted to simulate flows at the low Reynolds numbers ( $Re < 10^4$ ), in order to extract the airfoil sectional aerodynamic coefficients. Low Reynolds number airfoil decks,  $c_l, c_d, c_m$ , for the Mars rotor airfoil, 6% camber 2% thick cambered plate, were constructed. The computational fluid dynamics tool used is a Reynolds-averaged Navier-Stokes solver, Transonic Unsteady Rotor Navier-Stokes 2D (TURNS2D), developed at the University of Maryland. Figure 14 shows sample results of the lift to drag ratio over an angle of attack range for a sweep of Reynolds numbers at a constant Mach number. A broad range of conditions were tested to ensure complete

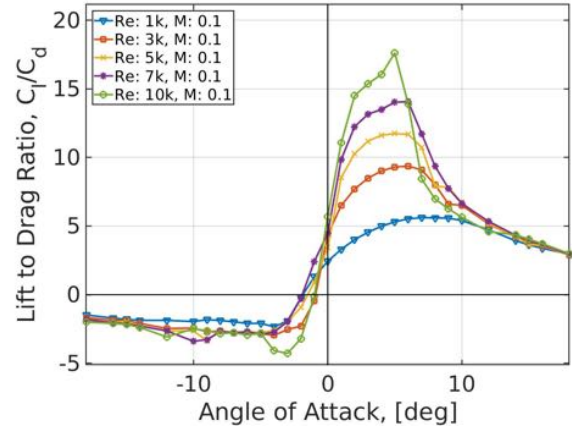


Fig. 14: Lift to Drag Ratio variation with Reynolds number at  $M=0.10$

coverage of the rotor operating conditions. A more detailed description of the methodology and results can be found in [15]

## 2.4. High Fidelity CFD

The aerodynamic model used in this analysis is the in-house University of Maryland framework Mercury, with the primary solver being Garfield, GPU-Accelerated Rotor Flow Field. Garfield is a structured finite-volume solver for the Reynolds Averaged Navier-Stokes (RANS) equation. Turbulence was accounted for with the Spalart-Allmaras (SA) turbulence model. Fifth order spatial accuracy and a CFL number of 5.0 was used with a time step size of a quarter of a degree of rotor azimuth,  $\Delta\Psi = 0.25^\circ$ .

An overset mesh was used. All blades used the same O-O mesh, and were offset by both height and azimuth at run time. The blades were completely enclosed by a tight nested rotor mesh, that had cell spacing of  $0.2c$  blade root chords, so that all the grid motion and re-connectivity would be limited to one mesh and increase speed of computation. Three more layers of nested meshes were used with constant spacing inside each, but with incremental grid growth between the layers, up to an outer cell spacing of  $5c$  blade root chords. The overset mesh system is shown in figure 16. The mesh extends a total distance of  $87c$  blade root chords in the plane of the rotor and  $68c$  blade root chords in the vertical direction. Each blade mesh had 2.9 million points with a total mesh size of 21 million points.

In addition to this validation, check runs were carried out to compare the coupled CFD/CA analysis for the Mars rotor by using the CREATE AV Helios framework, with completely different CFD and CA tools. Helios was ran with the same rotor geometry and flight conditions. Helios used a dual solver approach. The near body solver was a semi-structured strand solver, mStrand. For the off-body solver, a Cartesian solver, SAMCART was used. Pundit was used for the interface between the two solvers, and the MELODI module was employed to conduct the grid motion and communicate with the structural solver Rotorcraft Comprehensive Analysis System (RCAS). Helios and RCAS already had a coupling module and been extensively used in a variety of CFD/CA coupling applications.



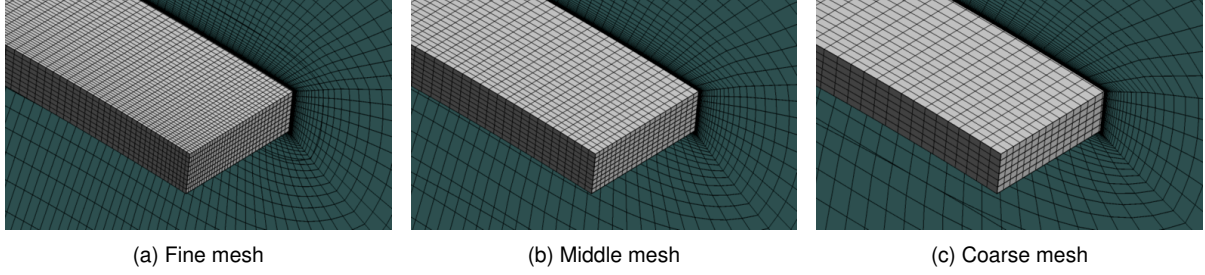


Fig. 15: Close up of blade tip for each mesh used in grid convergence study

Table 2: CFD Grid Convergence

Grid	Total Points	Time/step	Normalized F of M
Fine	24 million	33.58 s	1.000
Medium	21 million	21.54 s	0.979
Coarse	19 million	16.73 s	0.927

The atmospheric and flight conditions, as well as the rotor structural properties were matched between the two sets of analyses. One overset grid system was used in both tools, but with different implementations. Helios uses an Adaptive Mesh Refinement (AMR) that was set for up to 15 levels of refinement, isolated around the rotor wake, this way all the complex flow can be well captured while minimizing runtime costs by having cell refinement in unnecessary locations. The near body meshes are semi-structured and structured for Helios and Mercury, respectively, but similar grid resolution was set. The Mercury blade mesh cell sizes at the boundary wall and at the outer limit were set to be the same as the Helios grid, which was generated at run time by mStrand. The blade mesh resolution was chosen by a grid convergence study. A summary of the best blade grids, parameters and results, are given in table 2. As the wall normal spacing decreases, we see an increase in number of points, which increases run time. The metric used for comparing the grids was a normalized figure of merit, where the finest mesh was assumed to be accurate. Therefore to minimize runtime but maintain accuracy the medium mesh with a wall normal spacing of 0.001 was selected because it provided a significant runtime reduction while producing similar a figure of merit value.

A set of collective sweeps were performed at the same conditions as experimentally tested in the vacuum chamber to provide validation of proper model setup. Results for collective sweeps from  $-10^\circ$  to  $40^\circ$ , at  $5^\circ$  increments at two tip Reynolds numbers, 3,000 and 10,000, will be presented in the results.

## 2.5. High Fidelity Coupled CFD/CA Analysis

Delta-coupling between the aerodynamic and structural solvers was implemented to achieve a trim solution in forward flight. The structural solver calculates elastic deflections under airloads, and the aerodynamic solver calculates airloads for the given deflections. Baseline elastic deflections are passed to the aerodynamic solver for higher order airloads, which are then used to calculate updated deflections. These updated deflections are again passed into the aerodynamic solver to re-calculate the airloads. This

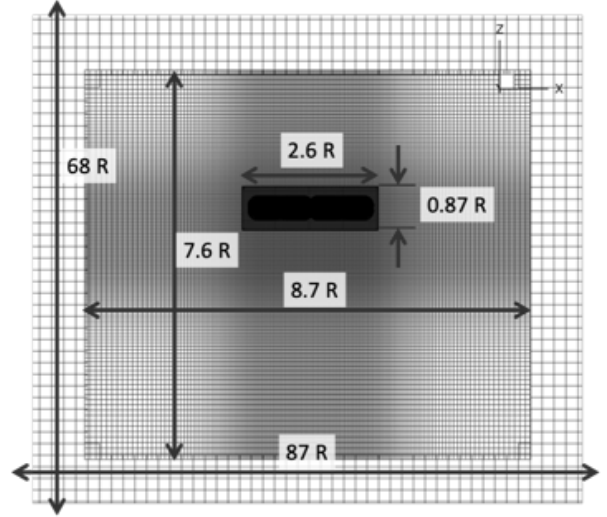


Fig. 16: Mercury CFD solver overset mesh organization

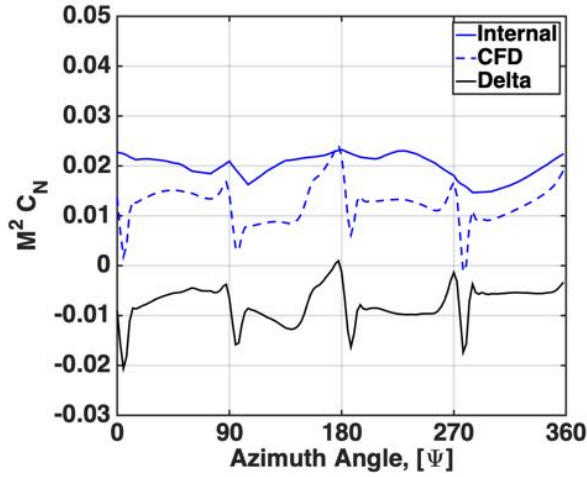
process is repeated until the deflections and airloads converge. Deflections were calculated at an azimuthal resolution of  $\Delta\Psi = 2.5^\circ$ . The CFD solver interpolates between these points and passes back airloads at an azimuthal resolution of  $\Delta\Psi = 0.25^\circ$ . Two full revolutions of CFD were completed for the first coupling iteration, to help develop the flow, but for the remaining iterations a single revolution was adequate. Convergence of the control angles was achieved after five coupling iterations, or six total CFD revolutions.

The key component of the delta-coupling algorithm is to correct the lower order CA airloads with a delta between CFD and CA airloads while retaining the damping airload sensitivity of the lower order airloads. This allows the internal airloads to change and converge towards trim while the delta airloads remain fixed for each coupling iteration. An sample of the delta airloads for the rotor normal force at the end of a CA trim is shown in figure 17. It can be seen that the waveform from the CFD airloads are successfully passed into the CA through the delta airloads.

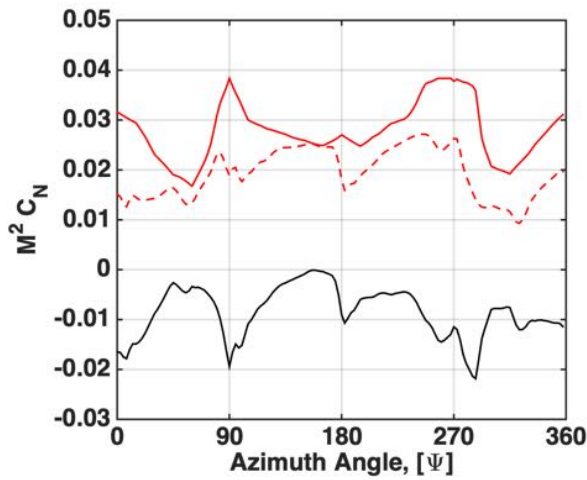
## 3. RESULTS

### 3.1. Validation with Single Rotor Hover Data

A single rotor model was developed and a collective sweep from  $-10^\circ$  to  $40^\circ$  at  $5^\circ$  increments was completed for tip Re of 3,000 and 10,000. Isolated CFD was adequate with prescribed blade deflections from the baseline CA model, for



(a) Upper rotor normal force coupling



(b) Lower rotor normal force coupling

Fig. 17: Sample sectional airload coupling through the delta method @75%R

these validation results. A sample solution with a collective of  $40^\circ$  at a tip Re of 10,000 is shown in figure 18. It can be seen that the large tip vortex is well tracked by the AMR software, which provides grid refinement around the rotor wake. The root vortex is weak and does not propagate far. The corresponding force history for this collective sweep is shown in figure 19. After two rotor revolutions, the solution has converged well. For the higher collective settings  $\theta = 30^\circ$  and  $40^\circ$ , the solution is not steady, but it has converged. These high collectives experience flow separation and re-attachment which has a strong influence on the rotor performance.

The comparison with experimental data is done in figure 20. Experimental data, baseline CA with lifting-line aerodynamics, and in-house CFD with prescribed deformations are compared in a single chart. For a tip Re of 10,000 both sets of analysis predict the experiment very well and only have a few small discrepancies as the blade approaches stall. As for the tip Re of 3,000, the CFD analysis over predicts the experimental data, while the baseline CA has a better prediction. These differences can be more easily seen in the performance metric of Figure of Merit,

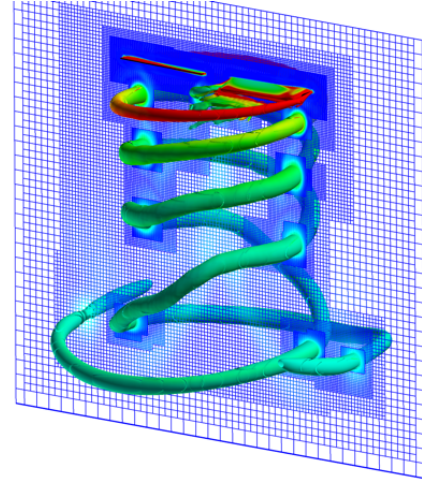


Fig. 18: Example single main rotor Helios CFD simulation at  $20^\circ$  and tip Re of 10,000. The solution is an iso-surface of Q-criterion, 0.03 and is colored by vorticity.

as shown in figure 21. The accurate prediction of 10,000 and over prediction of the the 3,000 tip Re, is clear. The trends are similar between the two sets of analysis, and in order to verify the accuracy of both these models, the same cases were ran with the US Army Helios code. The results are shown in figure 22. There are minor differences between the results. Helios predicts greater drag, and therefore power, compared to the in-house Mercury code, for both tip Reynolds number conditions. Additionally, Helios predicts a greater difference between the two cases, with the 3,000 tip Reynolds number having lower performance, while Mercury predicts similar results.

Flow field images for the difference blade collectives are shown in figures 24 and 23. For collectives of  $10^\circ$  and  $20^\circ$ , the flow is steady. Only for the collective of  $10^\circ$  is the flow fully attached. At  $20^\circ$  collective, the flow separates fully and stays separated, effectively increasing the airfoil thickness. At the higher collective settings, unsteady flow begins to develop; first at the trailing edge and then travel along the chord towards the leading edge. The effects of the flow separation can be seen through their effect on the spanwise flow. Figure 24 shows the spanwise flow distribution originating at three radial stations. For collectives of  $10^\circ$  and  $20^\circ$ , the flow is steady and there is very little cross flow or 3D effects. For collectives of  $30^\circ$  and  $40^\circ$ , the flow is separated, causing a region of flow on the upper surface where the flow velocity is radial and its pushed out towards the blade tip. Phenomena such as radial flow cannot be captured with 2D CFD and look up tables.

In addition to the the experimental validation the Mercury and Helios simulations were compared with each other. Figure 25 shows the resultant rotor thrust for the two sets of analysis. The impulsive loading and waveform is very similar. Helios predicts a higher thrust value at the blade passage locations and a greater impulsive loading. For the lower rotor, Helios has a greater mean thrust value compared to Mercury.

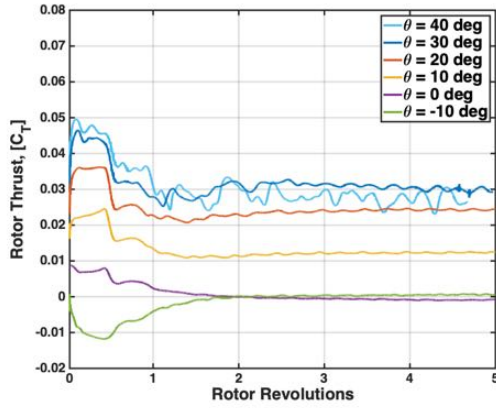


Fig. 19: Force history for computational CFD collective sweep at tip Re of 10,000

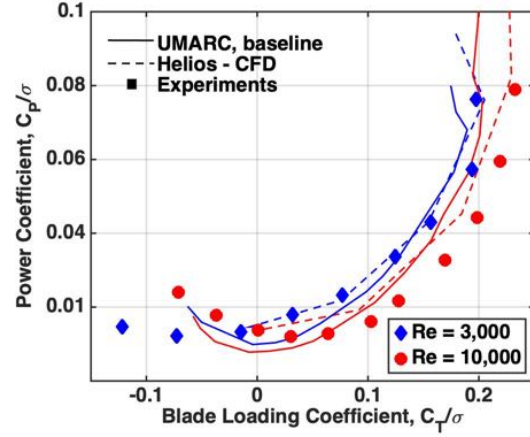


Fig. 22: Comparison of US Army Helios CFD and experimental results for sweeps at tip Re of 3,000 and 10,000

### 3.2. CFD/CA Coupled Analysis of Forward Flight

CFD/CA coupled analysis for both the hingeless and articulated rotor were carried out at an advance ratio  $\mu = 0.1$ , shaft angle of  $\alpha = 5^\circ$ , and blade loading of  $C_T/\sigma = 0.08$ . The CA (UMARC) had twenty spanwise structural beam finite elements and 12 time finite elements with deflections extracted precisely at  $2.5^\circ$  azimuthal resolution. The baseline aerodynamics used a non-linear nearwake and three revolutions of freewake. Each trim iteration took nearly 15 min on a single core. The Mercury CFD runs were conducted on the Maryland Advanced Research Computer Center (MARCC) cluster, Blue Crab. Each revolution took roughly 17 hours using four Nvidia K80 GPUs and 36 CPUs. The Helios CFD cases were ran on the Department of Defense's High Performance Computing DoD Supercomputing Resource Centers (DSRCs). Most cases were ran on the Topaz cluster on 540 CPUs. Each rotor revolution took around 8.5 hours.

The history of the integrated thrust and control angles over the coupling iterations show the success of the method for both rotor hubs. Detailed images of the converged flow field surrounding the rotor provides insight into the flow phenomena. The rotor airloads and deflections, reveal the necessity for the high fidelity analysis. The sectional bending loads and pitch link loads reveal insightful differences between a hingeless and articulated hubs for a Mars helicopter.

The control angle history over the five coupling iterations is shown in figure 26. The analysis is well behaved and the control angles change very little over the last three iterations. For both rotors, the baseline CA over predicted the thrust generated by 17.5%. Due to that offset, the coupling required an increase of blade collective, by an average of 17.1%. The lateral cyclic,  $\theta_{1c}$ , changes very little while the longitudinal cyclic,  $\theta_{1s}$ , increases in magnitude by 74.7%. The longitudinal cyclic is strongly influenced by the rotor wake, suggesting that the CFD wake is significantly different than the wake developed in the freewake analysis internal to the CA.

The coupling is well behaved and the thrust is nearly converged after three iterations, which can be seen in figure 27. For both rotor hubs, the upper rotor has a very large

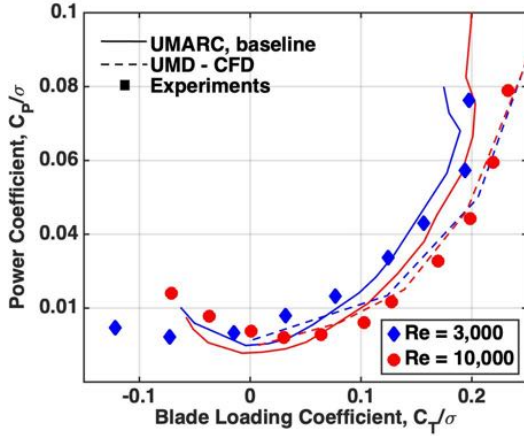


Fig. 20: Comparison of in-house analysis and experimental results for sweeps at tip Re of 3,000 and 10,000

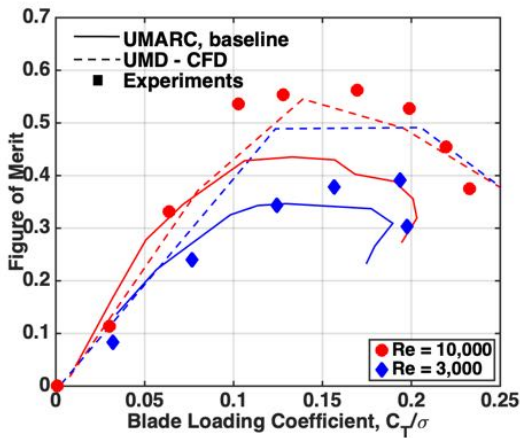
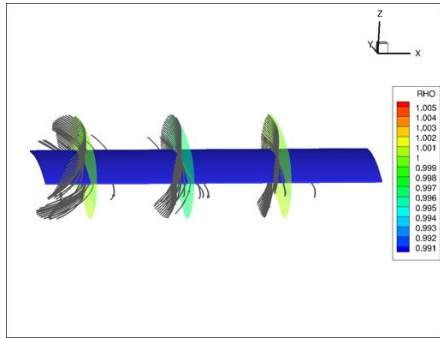
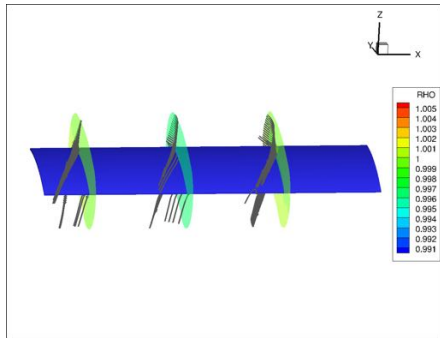


Fig. 21: Comparison of in-house analysis and experimental performance for sweeps at tip Re of 3,000 and 10,000

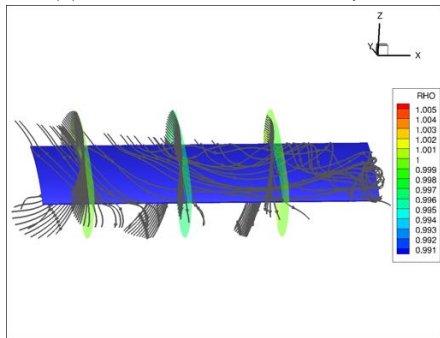




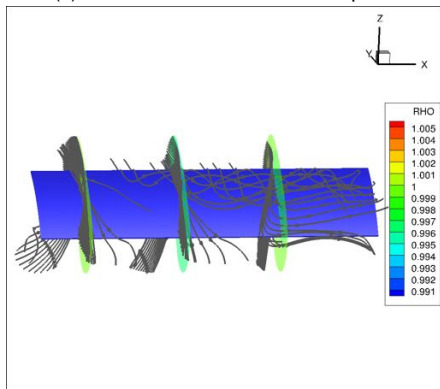
(a) Chordwise flow at 10° blade pitch



(b) Chordwise flow at 20° blade pitch

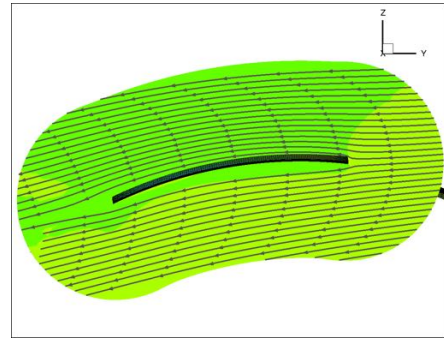


(c) Chordwise flow at 30° blade pitch

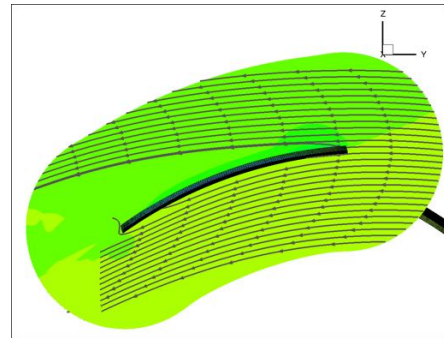


(d) Chordwise flow at 40° blade pitch

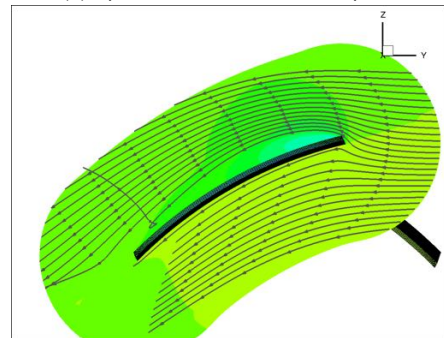
Fig. 23: Spanwise flow on single blade across of variation of blade pitches



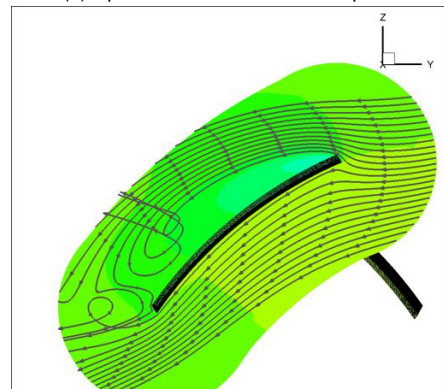
(a) Spanwise flow at 10° blade pitch



(b) Spanwise flow at 20° blade pitch



(c) Spanwise flow at 30° blade pitch



(d) Spanwise flow at 40° blade pitch

Fig. 24: Chordwise flow on single blade across of variation of blade pitches

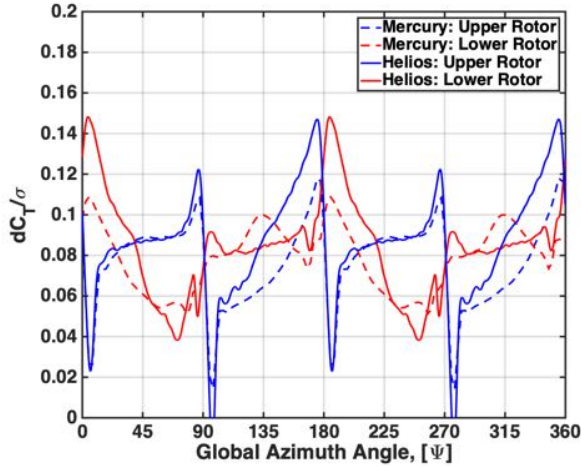


Fig. 25: Comparison of rotor thrust between the Helios/RCAS and Mercury/UMARC coupled analyses

4/rev impulsive loading while the impulsive loading on the lower rotor has a much smaller magnitude and the thrust is actually dominated by a large 2/rev forcing. The 4/rev loading on the upper rotor thrust is an effect of strong blade vortex interaction (BVI). As the lower rotor passes below the upper rotor, there is a large impact on rotor thrust that is not adequately captured by the lifting-line model. The UMARC thrust also shows a 4/rev loading, but with a significantly smaller magnitude. This phenomena is dominant in both the hingeless and articulated rotors. The lower rotor also sees a 4/rev loading, but with a much smaller magnitude and is dominated by the 2/rev forcing that is an effect of entering and leaving the upper rotor wake twice per revolution, on both advancing and retreating sides. UMARC begins to capture the 4/rev impulsive loading from wake but does not have the large 2/rev wake interaction on the lower rotor. A more detailed look at the flow phenomena of both rotors will be investigated with the help of CFD solution visualizations.

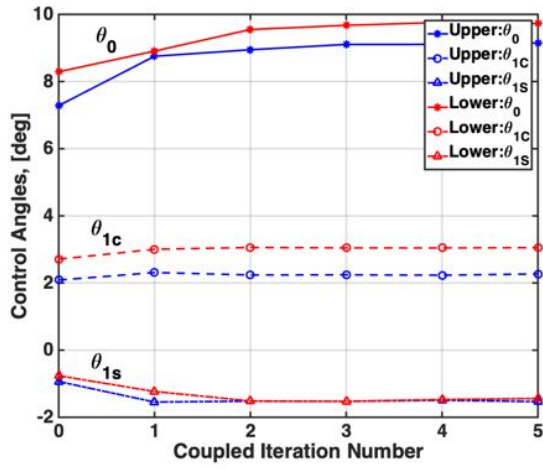
The converged CFD flow fields for both hingeless and articulated rotors are shown in figure 28. Iso-surface of Q-criterion (0.003) are plotted and colored by vorticity. The wake has the expected symmetric behavior but does not travel far behind the rotor and very quickly dissipates. This is due to two reasons: 1) for the given advance ratio, the upper rotor wake is ingested by the lower rotor which slices through the tip vortex causing a faster dissipation and 2) the high level of viscosity causes the vortices to lose energy and dissipates more quickly. There is no noticeable root vortex even without a center body. The root vortex might be too weak or destroyed by the interaction with the tip vortex and the high viscosity flow. Figure 29 shows the top and side views of the flow field. There are some subtle differences on the retreating side but over-all the nature of evolution, dissipation, and skew angles are very similar between the two rotors.

Figure 30 show the tip deflections for both the hingeless and articulated rotors, using both the baseline UMARC analysis and the coupled CFD/CA analysis. The colored lines represent the quarter chord position, and the band represents the entire blade chord length with the upper black line being the leading edge and lower black line as the trailing edge. The coupled CFD/CA analysis, shown in

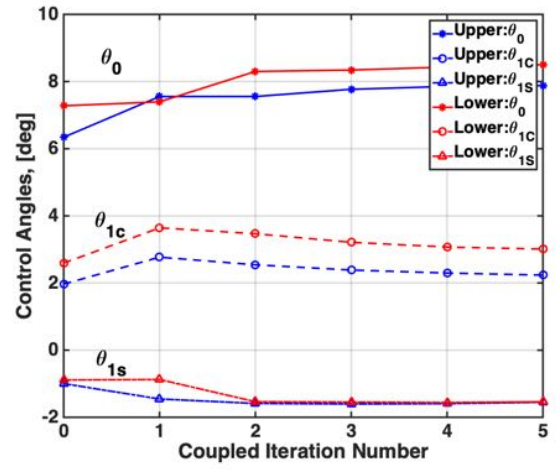
figures 30b and 30d, show the same waveform as the baseline analysis but with greater control angles and similar elastic deflections. Although the thrust was significantly increased, the effect on elastic deflection was negligible, with the larger effect on the lower rotors. Both rotors had only a marginal reduction in tip separation and therefore, blade strike chances. The four vertical lines at azimuths of  $\psi = 45^\circ, 135^\circ, 225^\circ$ , and  $315^\circ$  show the locations of blade passage. With rotor separation of  $10\%R$ , there is no concern for blade striking at these flight conditions. It is of note that the elastic deflection of the quarter chord is not sufficient measure of blade strike. The leading edge of the lower rotor and the trailing edge of the upper rotor should be considered instead. This is because of the large blade chord, necessitated by the Martian conditions. Conventionally an articulated rotor would be considered less ideal for a coaxial rotor because of its limitations on rotor separation due to greater flapping. This does not hold true on Mars. The minimum separation at blade passage locations is  $5.6\%R$  and  $5.9\%$  for the hingeless and articulated rotors, respectively. Although the articulated rotor has a greater flap angle, blade pitch is more important because of the large chord for the Mars rotor.

Due to the similarity in the airloads, as both rotors are trimmed to the same conditions, for clarity, only the hingeless airloads are shown in figure 31, but the necessary insights are apparent and applicable to both rotors. The airloads highlight the differences between the sets of analyses but do not distinguish the hingeless and articulated rotors apart from each other. As found with the integrated thrust, the baseline CA over predicts the sectional normal force, while also not capturing the total impulsive loading, especially for the upper rotor. The chordwise force is even more significantly under predicted. At all rotor azimuths, the drag force is nearly twice as great as predicted from CA lifting-line. The waveform is well captured with a steady offset. This is true for both upper and lower rotors. The baseline CA analysis cannot capture the complex flow, especially phenomena such as flow separation. The 2D look-up tables are steady. In the CFD analysis, the flow separates and reattaches, which significantly influences drag. While the waveform for the upper and lower rotor appear very different for the normal force, for the chordwise force, the waveform is very similar. For the pitching moment, there is an under prediction on the advancing side but not the retreating side, for either upper or lower rotor. For the upper rotor, the large impulsive loading occur in the pitching moments, which are not captured at all by the CA.

An important distinction between hingeless and articulated rotors is the sectional bending moments on the blades. The half peak-to-peak oscillatory bending moments for both the hingeless and articulated rotors are shown in figure 32. The oscillatory bending moments at three sections along the blade are shown in figure 33. While both the hingeless and articulated bending loads approach zero near the tip, only the articulated rotor approaches zero at the root end as expected. The more surprising fact is the only slight increase in maximum bending moment experienced by the hingeless rotor when compared to articulated. The maximum oscillatory flap bending moment of the hingeless rotor is only 6–7% greater than the articulated rotor, for both the upper and lower rotors. The lower rotors for both hub types

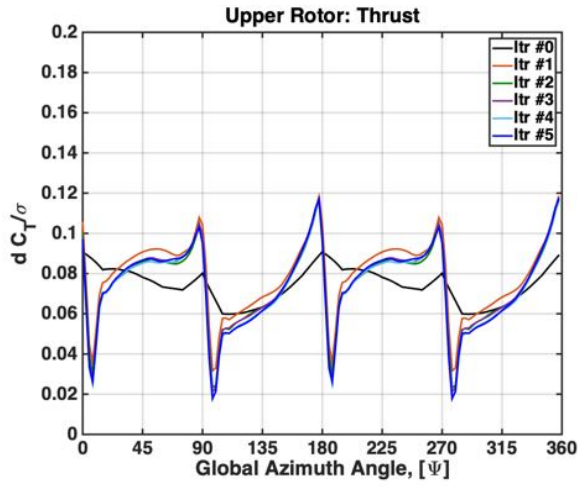


(a) Control angle history for hingeless rotor

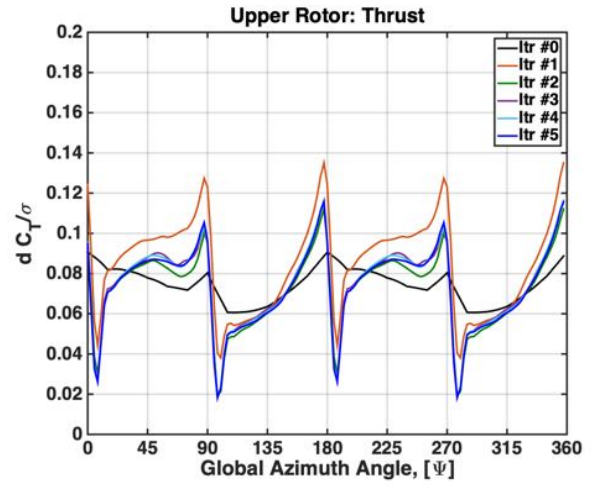


(b) Control angle history for articulated rotor

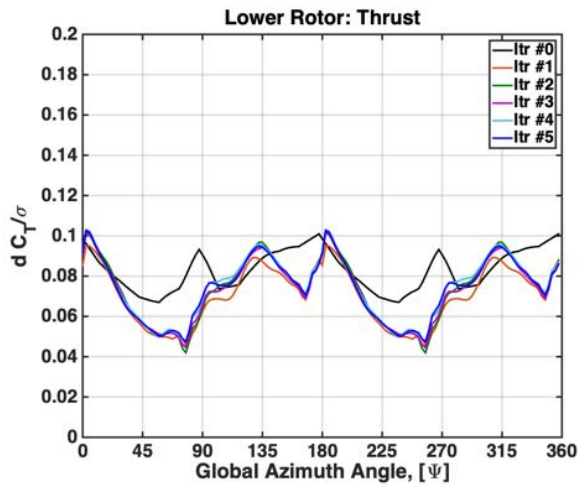
Fig. 26: Trimmed control angles for both rotors for CFD/CA convergence



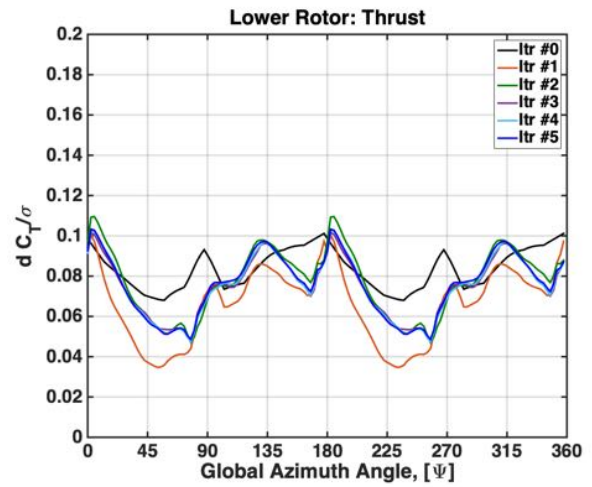
(a) Hingeless Upper Rotor



(b) Articulated Upper Rotor



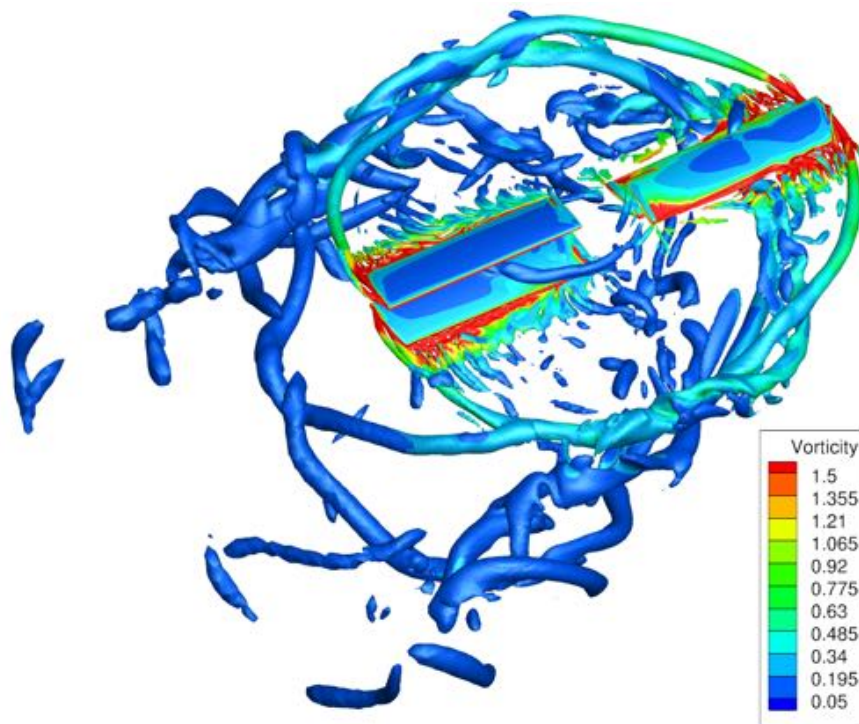
(c) Hingeless Lower Rotor



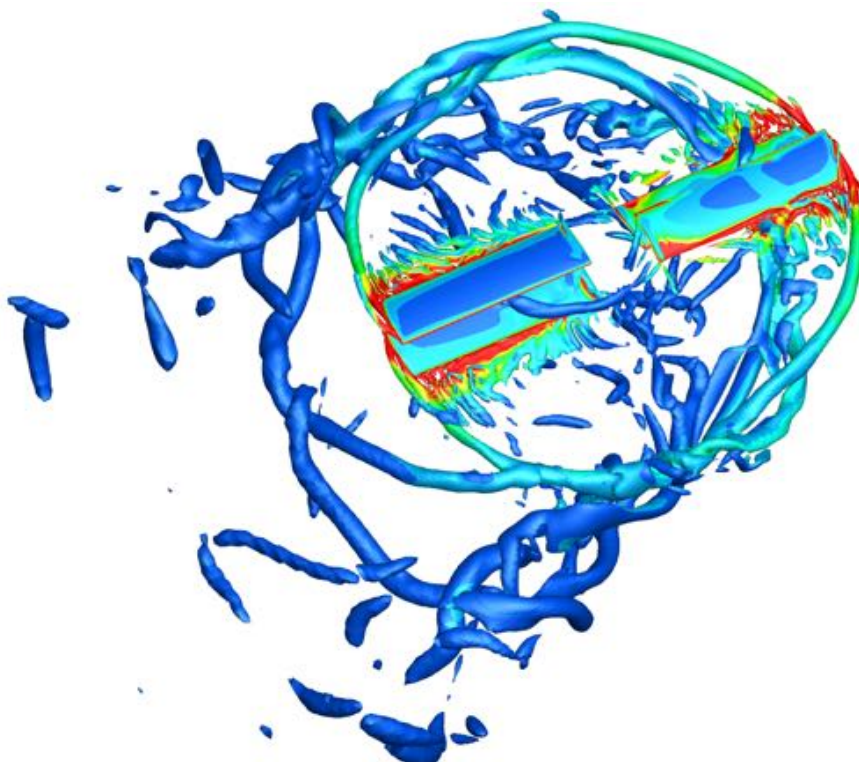
(d) Articulated Lower Rotor

Fig. 27: Airload convergence



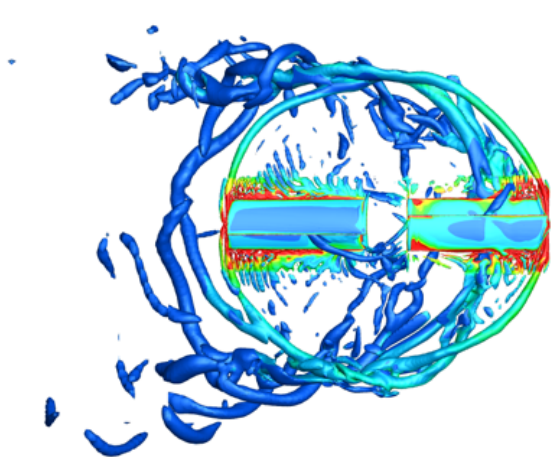


(a) Converged CFD solution for the hingeless rotor, isometric view

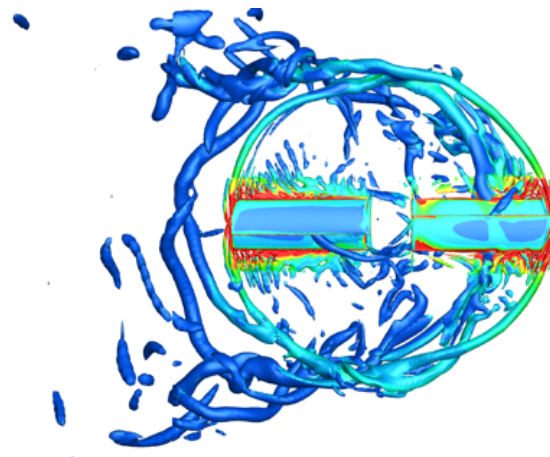


(b) Converged CFD solution for the articulated rotor, isometric view

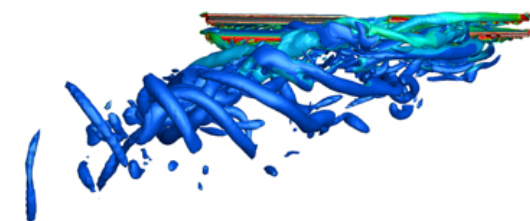
Fig. 28: Converged flow solutions for both rotors of iso-surface of Q-criterion, 0.03, that is colored by vorticity



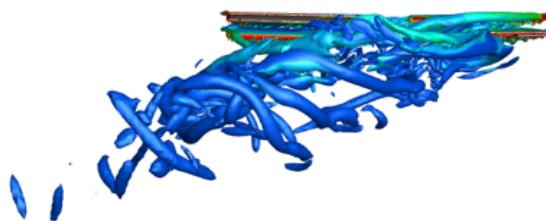
(a) Converged CFD solution for the hingeless rotor, top view



(b) Converged CFD solution for the articulated rotor, top view

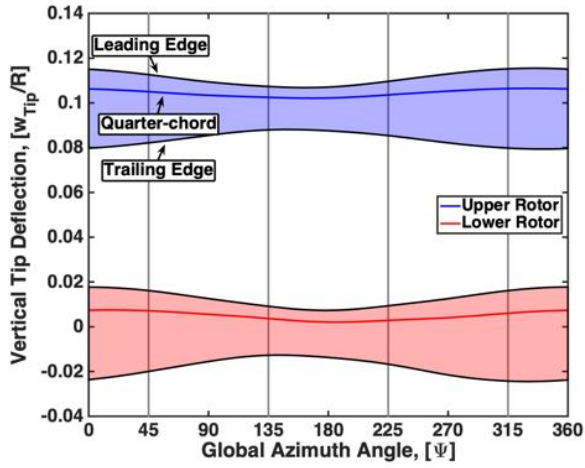


(c) Converged CFD solution for the hingeless rotor, side view

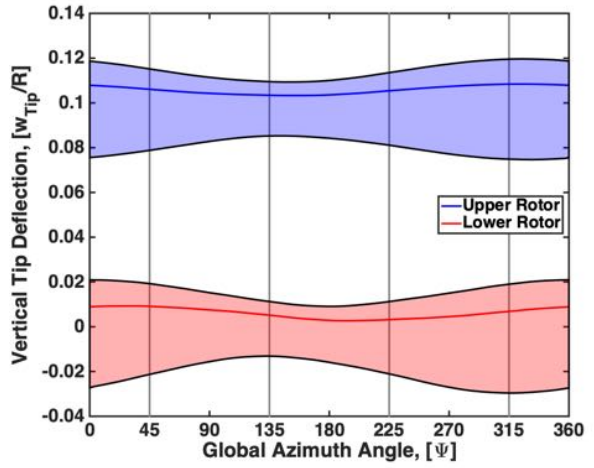


(d) Converged CFD solution for the articulated rotor, side view

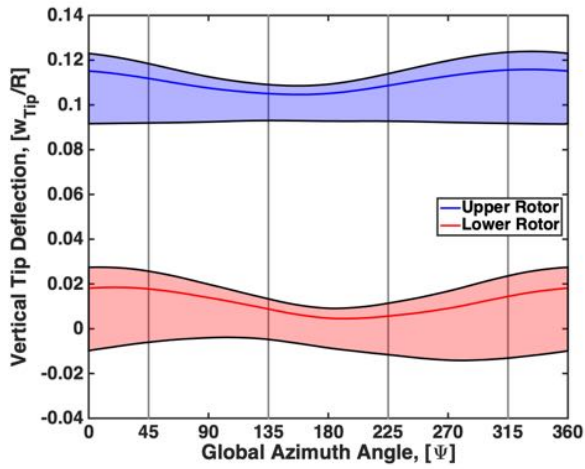
Fig. 29: Converged flow solutions for both rotors of iso-surface of Q-criterion, 0.03, that is colored by , top and side views



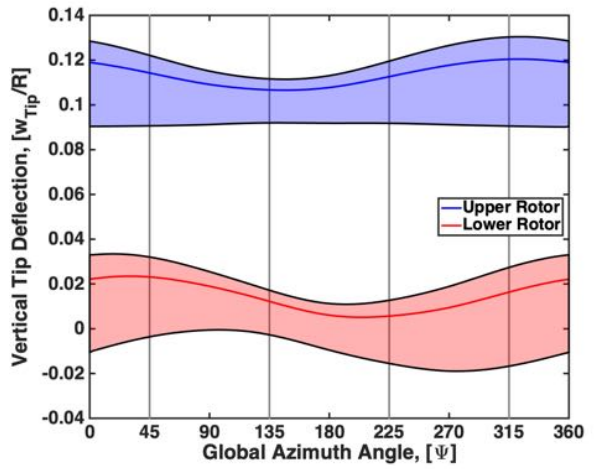
(a) Tip deflection for hingeless rotor from CA



(b) Tip deflection for hingeless rotor from CFD/CA



(c) Tip deflection for articulated rotor from CA



(d) Tip deflection for articulated rotor from CFD/CA

Fig. 30: Tip deflections including location of leading and trailing edges



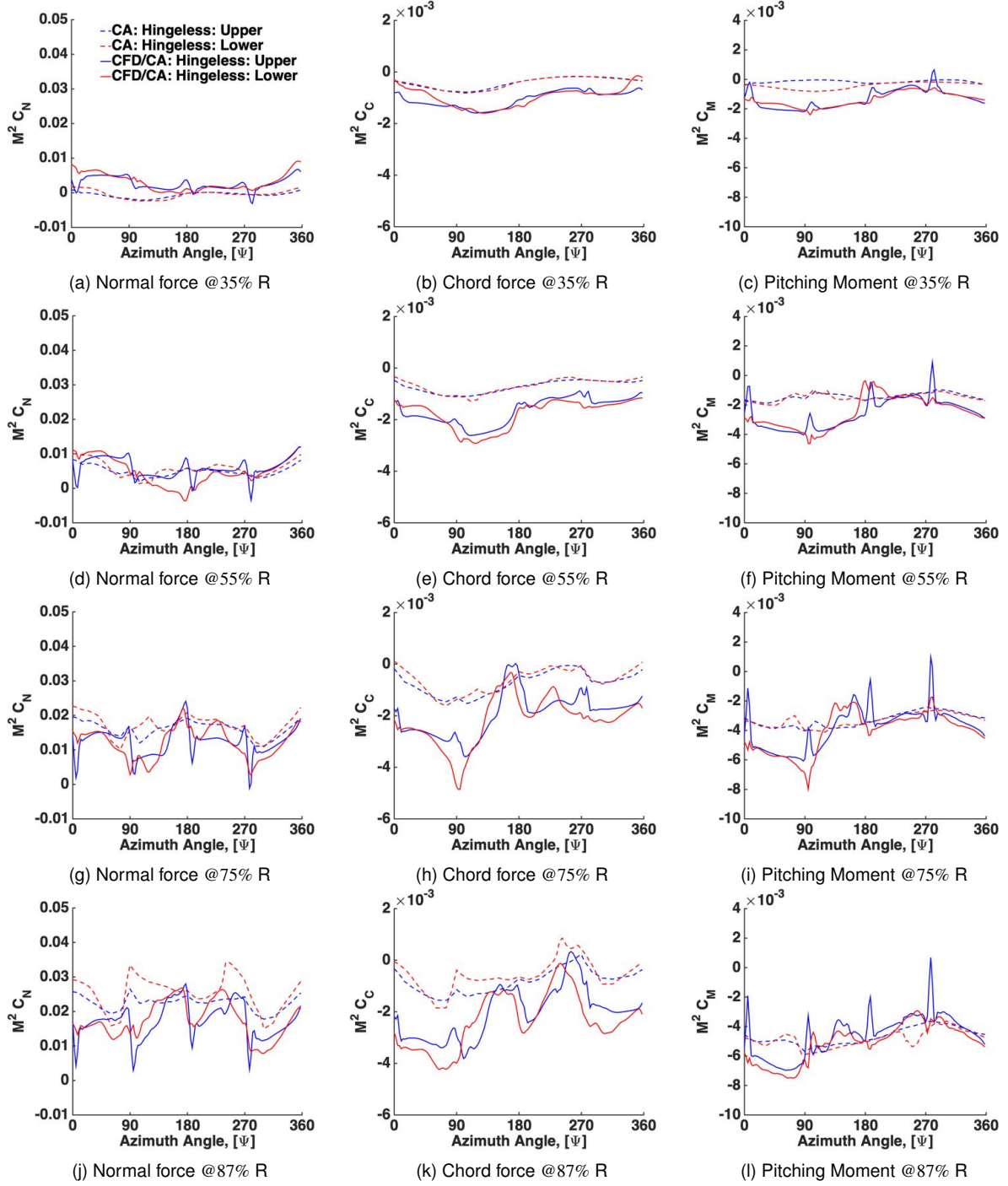
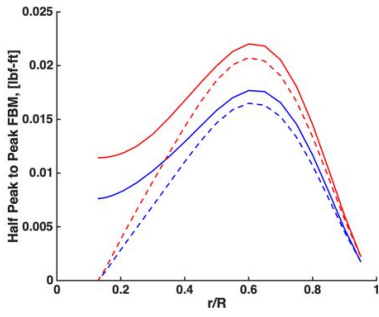
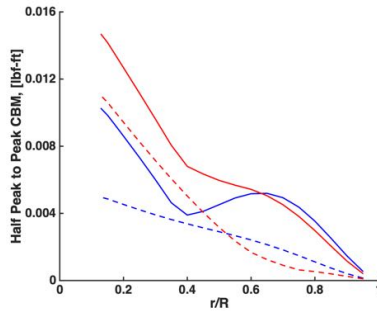


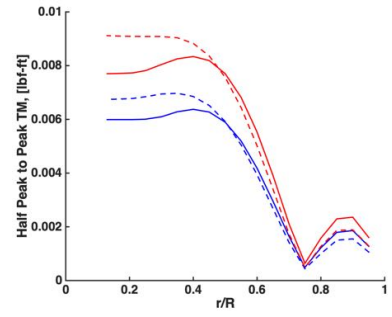
Fig. 31: Blade sectional forces for the hingeless rotor



(a) FBM peak to peak magnitude

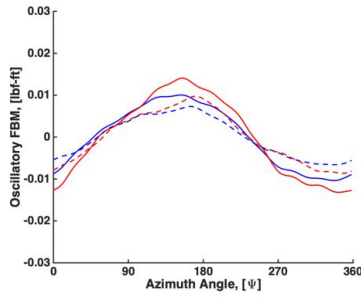


(b) CBM peak to peak magnitude

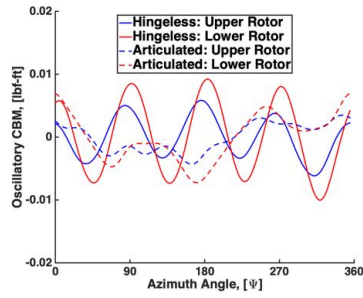


(c) TM peak to peak magnitude

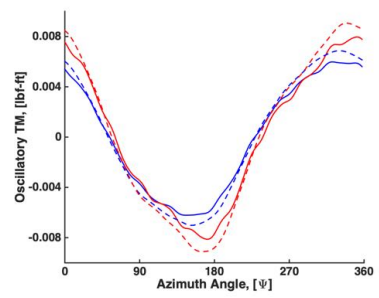
Fig. 32: Peak to Peak Loads



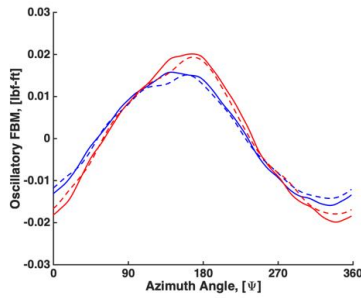
(a) Oscillatory FBM at @30% R



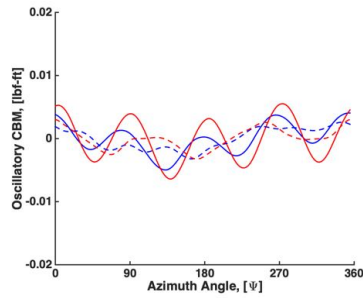
(b) Oscillatory CBM at @30% R



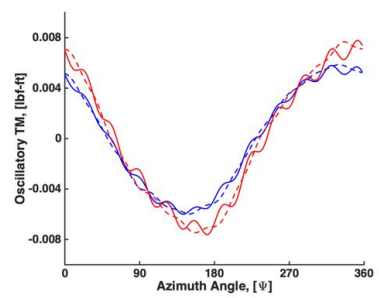
(c) Oscillatory TM at @30% R



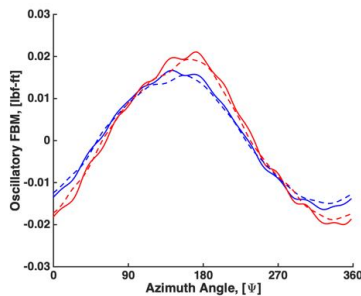
(d) Oscillatory FBM at @50% R



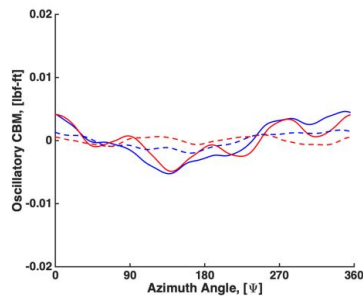
(e) Oscillatory CBM at @50% R



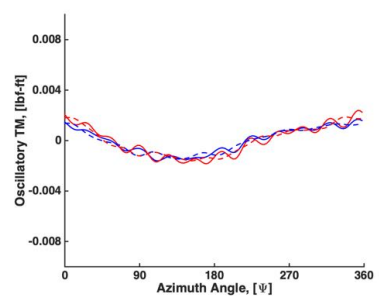
(f) Oscillatory TM at @50% R



(g) Oscillatory FBM at @70% R

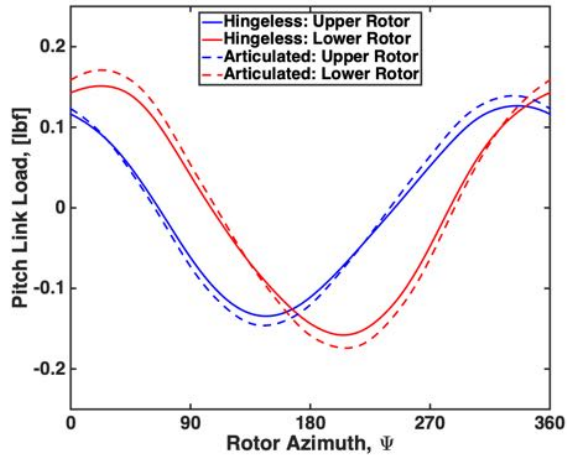


(h) Oscillatory CBM at @70% R

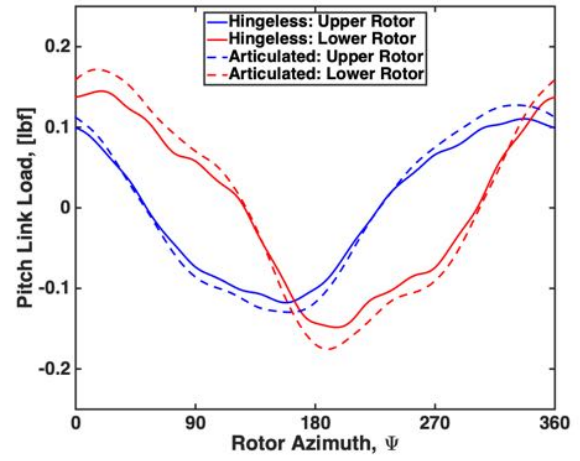


(i) Oscillatory TM at @70% R

Fig. 33: Blade sectional forces comparison between hingeless and articulated rotors

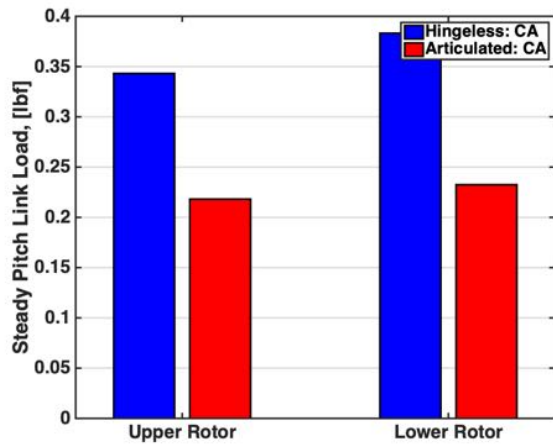


(a) Oscillatory pitch link loads from comprehensive analysis

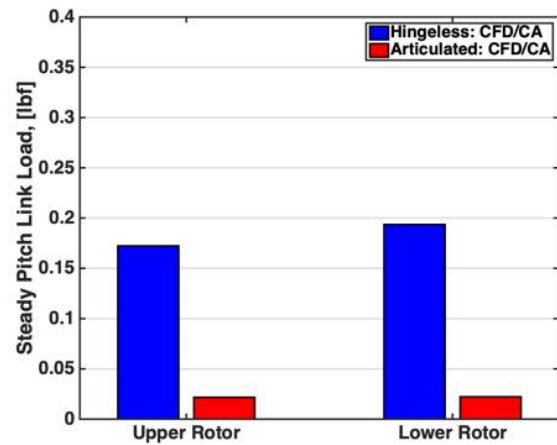


(b) Oscillatory pitch link loads from coupled analysis

Fig. 34: Oscillatory pitch link loads from both baseline and coupled CFD/CA analyses



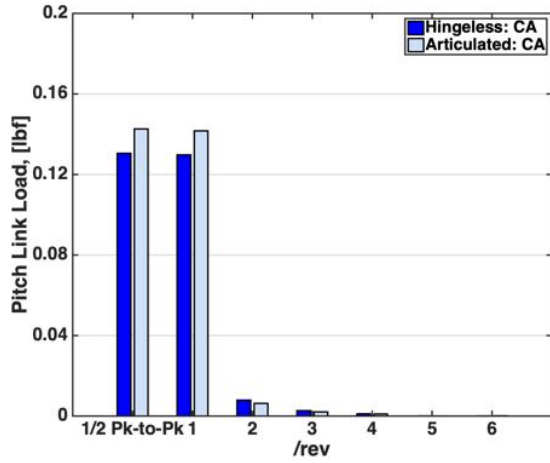
(a) Steady pitch link loads from comprehensive analysis



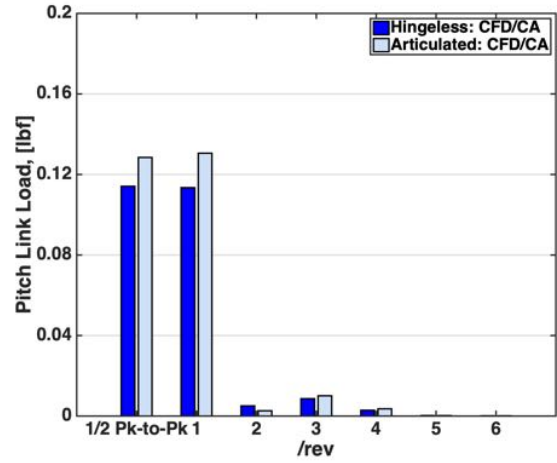
(b) Steady pitch link loads from coupled analysis

Fig. 35: Steady pitch link loads from both baseline and coupled CFD/CA analyses

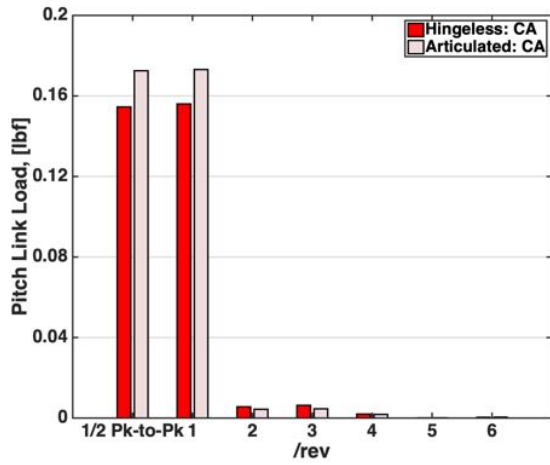




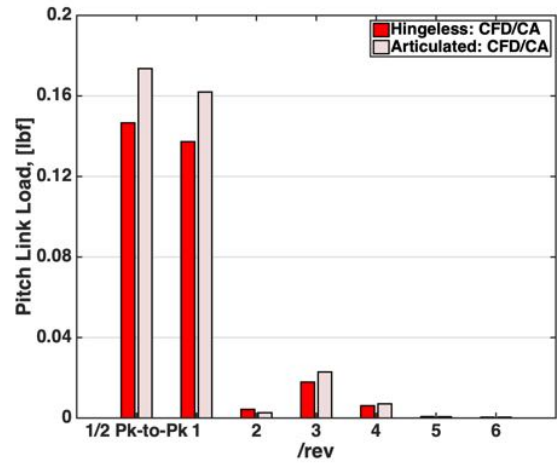
(a) Pitch link loads for both rotors from CA



(b) Pitch link loads for both rotors from CFD/CA



(c) Pitch link loads for both rotors from CA



(d) Pitch link loads for both rotors from CFD/CA

Fig. 36: Oscillatory pitch link loads, decomposed into each harmonics contribution

carry a more significant load than the upper rotors. From figure 33a, 33d, and 33g, the dominant flap loading along the entire blade span is 1/rev, but near the tip there are high frequency contributions. It was expected that the oscillatory flap bending moment on an articulated rotor would show significant reduction, but this is not the case. This means a hingeless rotor blade would not need substantially greater strength and weight on the blades. The flap bending moment is an especially crucial design parameter for the Mars helicopter because the low Re flow requires very thin blades, only 2% thickness to chord, and high flapwise loads would require a heavier, but also thicker blade, which would negatively impact the aerodynamics.

A high chord bending moment can be more easily accommodated because of the low aspect ratio, high chord length, blade design for the Mars rotor, but chord bending moment does show a more significant difference between the hingeless and articulated hubs. Similar to the flap bending, the lower rotor experiences larger chord bending moments, especially on the inboard half of the blade. The dominant frequency is 4/rev. The hingeless rotor is almost a pure 4/rev signal while the articulated also has a significant 1/rev. Although the hingeless rotor experiences larger chord bending moments, this difference is not great enough to decisively favor the articulated rotor.

The torsional moment produces the pitch link loads. Accounting for pitch link loads is important for sizing the control system, linkages and actuators. For such a small aircraft, large pitch link loads could cause a serious problem by requiring larger swashplate and control systems. The half peak-to-peak oscillatory torsion moment has a consistently high loading over the inboard 50% of the blade span, with a sharp reduction outboard. The articulated rotor carries a heavier load. This is due to the larger flap angles of the articulated rotor. Both the hingeless and articulated rotors are dominated by a 1/rev torsion moment. The hingeless rotor has visible higher harmonic contributions, whereas the articulated rotor does not. The articulated rotor has a marginally larger torsion moment than the hingeless rotor, but significantly higher pitch link loads.

The oscillatory pitch link loads, in figure 34b match the waveform from the torsional moment, and show a slightly larger peak-to-peak load. Figure 34 compares the oscillatory pitch link load between the baseline CA and coupled CFD/CA. The oscillatory loads between the two analysis show similar results. The coupled CFD/CA has more higher harmonics, but the inclusion of better wake do not have a significant impact. The oscillatory pitch link load is decomposed into harmonic contributions in figure 36. The dominant contribution is the 1/rev, but the coupled CFD/CA has larger contributions from 2, 3, and 4/rev. Figure 35 gives the steady values for the pitch link loads for both sets of analysis. The baseline CA significantly over predicts the pitching moment for both hingeless and articulated rotors, but captures the basic trend that the hingeless rotor has a much larger steady component, compared to the articulated rotor. This hingeless rotor would require a much stiffer and stronger control system than the articulated rotor because of the steady pitch link loading.

## 4. CONCLUSION

The present work focused on the development of a coupled CFD/CA of a coaxial Mars rotorcraft. It studied the effect of hub type, on performance, loads, and control loads. A high fidelity analysis is necessary because of the complex problem of coaxial rotors complicated farther by the atmospheric conditions of flying on Mars. Both the CFD and CA were independently validated with experimental data in hover for a single rotor tested in a vacuum chamber. The analysis was then extended to a coaxial rotor in forward flight. The baseline comprehensive analysis did not capture the impulsive aerodynamic loading from wake. Based on this study the following key conclusions are drawn: (1) The hingeless rotor requires greater pitch angles than the articulated rotor and hence exhibits less rotor separation, due to large chord on Mars, (2) the oscillatory bending moments are comparable between the two rotors. The hingeless rotor does experience greater flap bending moments but the difference is not as significant as on Earth. This is due to the dominance of centrifugal loading from higher rotational speed over the lift, (3) the articulated rotor has oscillatory pitch link loads 15.5% higher than the hingeless rotor, but (4) the hingeless rotor has steady pitch link loads of over 8 times the articulated rotor.

## 5. ACKNOWLEDGMENTS

The authors would like to thank Beatrice Roget, Roger Strawn, and the entire Helios Development team at the US Army ADD at the NASA Ames Research Center. Daniel Escobar is supported by the Clark Doctoral Fellowship Program

## 6. REFERENCES

- <sup>1</sup>Young, L., Gulick, V., and Briggs, G., "Rotorcraft as Mars Scouts," IEEE Aerospace Conference, Big Sky, MT, March 9-16 2002.
- <sup>2</sup>Young, L., Aiken, E., Derby, M., Demblewski, R., and Navarrete, J., "Experimental Investigation and Demonstration of Rotary-Wing Technologies for Flight in the Atmosphere of Mars," American Helicopter Society 58th Annual Forum, Montreal, Canada, June 11-13 2002.
- <sup>3</sup>Datta, A., Roget, B., Griffiths, L., Pugliese, G., Sitamaran, J., Bao, D., Liu, J., Gamard, O., "Design of a Martian Autonomous Rotary-Wing Vehicle," *Journal of Aircraft*, Vol. 40, (3), May-June 2003, pp. 461-472.
- <sup>4</sup>Corfeld, K., Strawn, R., and Long L., "Computational Aerodynamics Analysis of a Martian Rotorcraft," *Journal of the American Helicopter Society*, Vol. 49, (3), June 2003, pp. 350-356.
- <sup>5</sup>Shrestha, R., Benedict, M., Hrishikeshavan, V., and Chopra, I., "Hover Performance of a Small-Scale Helicopter Rotor for Flying on Mars," *Journal of Aircraft*, Vol. 53, (4), July-August 2016, pp. 1160-1167.
- <sup>6</sup>Balaram, J., Canham, T., Duncan, C., Golobek, M., Grip, H., Johnson, W., Maki, J., Quon, A., Stern, R., Zhu, D., "Mars Helicopter Technology Demonstrator," Paper 0023, AIAA SciTech Forum, Kissimmee, FL, January 2018.

<sup>7</sup>Grip, H, Scharf, D., Malpica, C., Johnson, W., Mandic, M., Singh, G., Young, L., “Guidance and Control for a Mars Helicopter,” Paper 1849, AIAA SciTech Forum, Kissimmee, FL, January 2018.

<sup>8</sup>Savu, G., and Trifu, O., “Photovoltaic Rotorcraft for Mars Missions,” 31st AIAA/ASME/SAE/ASEE Joint Propulsion Conference and Exhibit, San Diego, CA, July 10-12 1995.

<sup>9</sup>Young, L., Aiken, E., Derby, M., Demblewski, R., and Navarrete, J., “Design Opportunities and Challenges in the Development of Vertical Lift Planetary Aerial Vehicles,” American Helicopter Society International Vertical Lift Aircraft Design Specialist’s Meeting, San Francisco, CA, January 19-21 2000.

<sup>10</sup>Datta, A., Bao, J., Gamard, O., Griffiths, D., Liu, L., Pugliese, G., Roget, B., Sitamaran, J., “The Martian Autonomous Rotary-Wing Vehicle (MARV),” American Helicopter Society Student Design Competition Report, 1 June 2000.

<sup>11</sup>Winslow, J., Otsuka, H., Govindarajan, B., and Chopra, I., “Basic Understanding of Airfoil Characteristics at Low Reynolds Numbers ( $10^4$ – $10^5$ ),” *Journal of Aircraft*, Vol. 55, (3), December 2017, pp. 1050–1061.

<sup>12</sup>Grip, H., Lam, J., Bayard, D., Conway, D., Singh, G., Brockers, R., Delaune, J., Matthies, L., Malpica, C., Brown, T., Jain, A., San Martin, A., Merewether, G., “Flight Control System for NASA’s Mars Helicopter,” Paper 1289, AIAA SciTech Forum, San Diego, CA, January 2019.

<sup>13</sup>Bayard, D., Conway, D., Brockers, R., Delaune, J., Matthies, L., Grip, H., Merewether, G., Brown, T., San Marin, A., “Vision-Based Navigation for the NASA Mars Helicopter,” Paper 1411, AIAA SciTech Forum, San Diego, CA, January 2019.

<sup>14</sup>Pipenberg, B., Keennon, M., Tyler, J., Langberg, S., Hibbs, B., Balaram, J., Grip, H., Pempejian, J., “Design and Fabrication of the Mars Helicopter Rotor, Airframe, and Landing Gear Systems,” Paper 0620, AIAA SciTech Forum, San Diego, CA, January 2019.

<sup>15</sup>Escobar, D., Chopra, I., and , Datta, A., “Aeromechanical Loads on a Mars Coaxial Rotor,” AHS 74th Annual Forum, Phoenix, AZ, May 2018.

<sup>16</sup>Escobar, D., Chopra, I., and , Datta, A., “Vacuum Chamber Testing of 1.5-Foot Diameter Mars Rotor,” AHS Technical Conference on Aeromechanics Design for Transformative Vertical Flight, San Francisco, CA, January 2018.